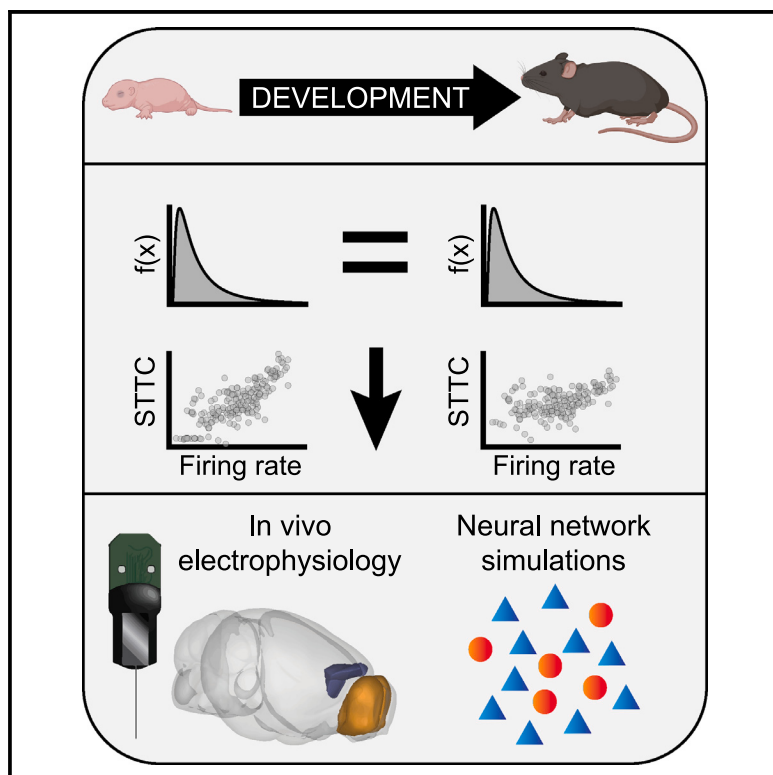


## Preconfigured architecture of the developing mouse brain

### Graphical abstract



### Authors

Mattia Chini, Marilena Hnida,  
Johanna K. Kostka, Yu-Nan Chen,  
Ileana L. Hanganu-Opatz

### Correspondence

mattia.chini@zmnh.uni-hamburg.de

### In brief

Chini et al. show that the distribution shape of single-unit-related parameters is largely stable across the early development of cortical circuits. Using computational modeling, they predict that synaptic parameters have similar dynamics. Thus, they conclude that this aspect of cortical organization is preconfigured and experience independent.

### Highlights

- Single-unit parameters have a right-skewed and heavy-tailed distribution across development
- Synaptic parameters with this type of distribution are needed to stably model the data
- In early development, neurons display an oligarchical organization that decreases with age
- Inhibitory synaptic plasticity recapitulates the decrease in the oligarchical organization



## Article

Preconfigured architecture  
of the developing mouse brainMattia Chini,<sup>1,2,\*</sup> Marilena Hnida,<sup>1</sup> Johanna K. Kostka,<sup>1</sup> Yu-Nan Chen,<sup>1</sup> and Ileana L. Hanganu-Opatz<sup>1</sup><sup>1</sup>Institute of Developmental Neurophysiology, Center for Molecular Neurobiology, University Medical Center Hamburg-Eppendorf, Hamburg, Germany<sup>2</sup>Lead contact

\*Correspondence: mattia.chini@zmnh.uni-hamburg.de

<https://doi.org/10.1016/j.celrep.2024.114267>

## SUMMARY

In the adult brain, structural and functional parameters, such as synaptic sizes and neuronal firing rates, follow right-skewed and heavy-tailed distributions. While this organization is thought to have significant implications, its development is still largely unknown. Here, we address this knowledge gap by investigating a large-scale dataset recorded from the prefrontal cortex and the olfactory bulb of mice aged 4–60 postnatal days. We show that firing rates and spike train interactions have a largely stable distribution shape throughout the first 60 postnatal days and that the prefrontal cortex displays a functional small-world architecture. Moreover, early brain activity exhibits an oligarchical organization, where high-firing neurons have hub-like properties. In a neural network model, we show that analogously right-skewed and heavy-tailed synaptic parameters are instrumental to consistently recapitulate the experimental data. Thus, functional and structural parameters in the developing brain are already extremely distributed, suggesting that this organization is preconfigured and not experience dependent.

## INTRODUCTION

In the adult brain, many structural and functional parameters follow right-skewed distributions with heavy right tails, such as the log-normal,<sup>1,2</sup> gamma,<sup>3</sup> or power law<sup>4,5</sup> distribution. A non-exhaustive list of parameters that is characterized by such distributions includes size and number of synapses<sup>6–9</sup>; size of post-synaptic currents<sup>10–12</sup>; diameter of axons<sup>13</sup>; density of neurons<sup>14</sup>; *in vivo* single-unit-activity (SUA) firing rates<sup>15–17</sup>; spike transmission probability<sup>10,17</sup>; pairwise correlations among spike trains<sup>18</sup>; and power of the local field potential (LFP),<sup>19,20</sup> electroencephalogram (EEG),<sup>21–23</sup> magnetoencephalogram (MEG),<sup>22–24</sup> and blood-oxygen-level-dependent (BOLD)<sup>25</sup> signals.

If a parameter follows such a distribution, it is implied that a large proportion of the data display small values that fall well below the mean. Conversely, extremely large values are more commonly observed than if they followed a narrower distribution such as the normal (or Gaussian), as is often implicitly assumed.<sup>1,2</sup> Thus, these distributions are characterized by high levels of inequality. We define such distributions as being “extreme.”<sup>26</sup> It has been suggested that the extreme distribution of neural parameters might have several useful properties.<sup>1,2,10,27</sup> For instance, the log-normal distribution of synaptic sizes might promote the formation and propagation of neuronal sequences,<sup>10,28</sup> while at the same time optimizing storage capacity.<sup>27</sup> Moreover, the extreme distribution of firing rates might result in an environment with an optimal balance between a large amount of “specialist” neurons complemented by few “generalists.” The first ones would only fire upon receiving a

highly specific constellation of pre-synaptic inputs, and thereby have a spiking activity with unique and distinctive “interpretation” for post-synaptic partners. Conversely, generalist neurons would require less specific pre-synaptic inputs to generate a spike. This could allow such neurons to generalize over similar sensory stimuli and might therefore represent the brain’s “best guess.”<sup>1,2</sup> Overall, this organization is thought of producing a system that allows for concomitant specialization and flexibility, while limiting the number of energy-demanding high-firing-rate neurons.<sup>10</sup>

While it is widely accepted that the adult brain is an extreme environment, how this unfolds throughout development is still unclear. Two main competing hypotheses have been put forward. The “blank-slate model” posits that the developing brain is a *tabula rasa*, a blank slate that lacks a refined structure.<sup>29</sup> A corollary of this view is that structural and functional parameters in the developing brain should follow a narrow, thin-tailed distribution. Only upon developmental learning would the brain structure gradually become skewed, heavy tailed, and unequal, as reported for the adult brain. While this view is not often openly advocated for, it is often implied.<sup>2,30,31</sup> The competing theory is the “preconfigured brain hypothesis,” which proposes that the developing brain is pre-packaged with non-random structure and already displays extreme distributions of structural and functional parameters. Consequently, this hypothesis implies that developmental learning should not fundamentally transform the brain architecture. Rather, learning is viewed as a matching process that associates pre-existing structure, which is



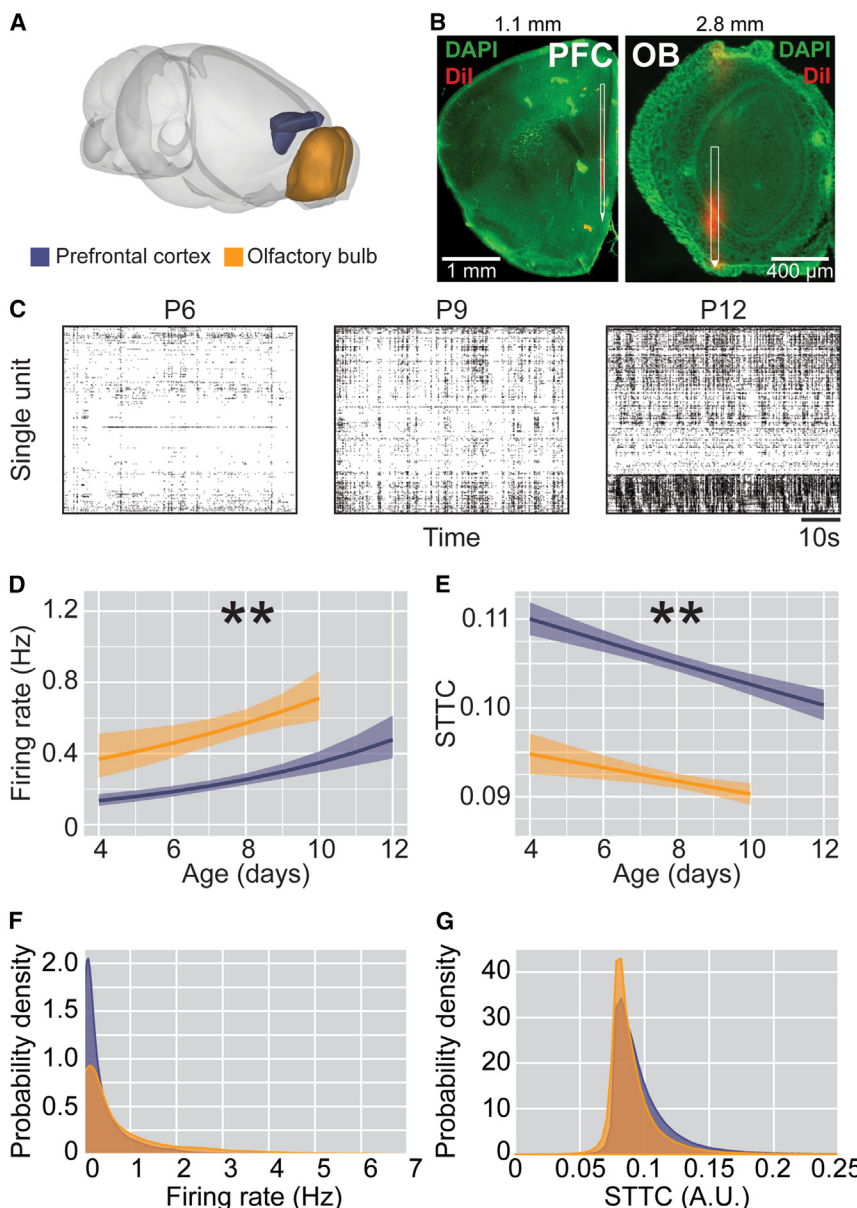


**Figure 1. SUA firing statistics in the mouse PFC and OB across the first two postnatal weeks**

(A) Schematic representation<sup>46</sup> of extracellular recordings in the PFC and OB of P4–12 mice.

(B) Digital reconstruction of the position of a Dil-labeled recording electrode in the PFC (left) and OB (right) with the antero-posterior distance from bregma (top) of a Nissl-stained coronal section (green) of a P9 and P10 mouse, respectively. Scale bar: 1 mm (left) and 400 μm (right).

(C) Representative raster plot of 1 min of SUA activity recorded in the PFC of a P6 (left), P9 (middle), and P12 (right) mouse.

(D) Line plot displaying the SUA firing rate of P4–12 mice ( $n = 278$  mice and 14,357 single units). Color codes for brain region.

(E) Same as (D) for STTC ( $n = 278$  mice and 654,335 spike train pairs).

(F) Probability density distribution for SUA firing rate in P4–12 mice. Color codes for brain region.

(G) Same as (F) for STTC. In (D) and (E) data are presented as mean and 95% confidence interval (CI). Asterisks in (D) and (E) indicate significant effect of age. \*\* $p < 0.01$ , generalized linear mixed-effect models.

the most protracted development.<sup>38</sup> We show that, in both brain regions, the skewness, tailedness, and inequality of the distributions of *in vivo* SUA firing rates and pairwise interactions among spike trains do not increase throughout development. Along the same lines, already midway through the first postnatal week, the PFC displays a non-random small-world topography. Moreover, in both brain regions, neurons in the right tail of the firing-rate distribution are overwhelmingly more likely to also be in the right tail of the pairwise interaction distribution and to exhibit hub-like properties. We refer to this organization as oligarchical, and we show that it

initially devoid of meaning, with a behavioral output or a sensory sensation.<sup>2,32–35</sup>

To tease apart these two hypotheses, we investigated the *in vivo* development of brain activity in a large-scale dataset from unanesthetized postnatal day (P) 4–60 mice ( $n = 302$  mice). The youngest mice in the dataset belong to a very immature developmental phase in which, even though neurons in the sensory systems are active, they mostly do not represent sensory information. An exception to this developmental dynamic is the olfactory system. From birth onward, rodents rely on olfaction for survival, as they actively employ olfactory cues to locate the dam's nipple.<sup>36,37</sup> Thus, in the present study, to control for the potential effect of developmental learning, we investigated the early developing olfactory bulb (OB) and the prefrontal cortex (PFC), the cortical region with

gradually wanes throughout adulthood, concomitantly with a maturation of excitation-inhibition balance.

## RESULTS

### SUA firing rate exponentially increases over age, while spiking activity decorrelates

To assess the *in vivo* developmental firing dynamics, we analyzed a large-scale dataset of SUA ( $n = 278$  mice, 14,357 units and 654,335 spike train pairs) recorded with Neuropixels as well as single- and multi-shank Neuronexus silicon probes from the PFC and the ventral OB of non-anesthetized P4–P12 mice ( $n = 278$  mice) (Figures 1A–1C and S1A–S1C). Some of the data have been used in previously published studies.<sup>39,40</sup> We calculated the firing rate (first-order SUA statistics) and the

spike-time tiling coefficient (STTC; second-order SUA statistics, calculated at a 10-ms timescale), a measure of pairwise correlation among spike trains that is not biased by firing rate.<sup>41</sup> In line with previous reports,<sup>39,40,42–45</sup> using multivariate linear regression, we found that firing rate exponentially increased with age in both brain regions (age effect = 0.11, confidence interval [CI] [0.04; 0.18],  $p = 0.004$ , generalized linear mixed-effect model) (Figure 1D) and that the OB displayed a higher firing rate than the PFC (firing rate at P8 = 0.57 and 0.25 Hz, CI [0.50; 0.65] and [0.22; 0.29] for OB and PFC, respectively,  $p < 10^{-16}$ ) (Figures 1D and S1D).

Concomitant with the increase of firing rate, and consistent with previously published data,<sup>39,47,48</sup> the STTC exponentially decreased with age (age effect = −0.008, CI [−0.014; −0.003],  $p = 0.003$ , linear mixed-effect model), indicating a developmental decorrelation of spiking activity (Figure 1E). When evaluating this effect on individual brain regions, we found that the OB displayed lower STTC values than the PFC (STTC value at P8 = 0.092 and 0.105, CI [0.091; 0.093] and [0.104; 0.106] for OB and PFC, respectively,  $p < 10^{-16}$ ) (Figures 1E and S1E).

Lastly, when pooled across mice and brain regions, both firing rate and STTC already displayed a right-skewed and heavy-tailed distribution at these early developmental stages (Figures 1F and 1G).

These data indicate that, in both brain regions, SUA firing rates exponentially increase across the first two postnatal weeks while, at the same time, spiking activity decorrelates. Consistent with the early maturation of the OB and its high density of INs,<sup>37</sup> the OBs display higher firing rates and lower STTC values than the PFCs. Even at neonatal age, the two variables exhibit a right-skewed and heavy-tailed distribution in both brain areas.

### The skewness, tailedness, and inequality of the SUA firing statistics do not increase over age

A corollary of the blank-slate model is that the distributions of functional parameters should become more extreme over development. To quantify the distribution shape for the first- and second-order SUA statistics, we computed their skewness, kurtosis, and Gini coefficient (Figures 2A–2C). Skewness and kurtosis are the third and fourth central moments of a variable, and they measure its asymmetry and tailedness, respectively. Negative values of skewness indicate a left-skewed distribution, positive values a right-skewed distribution, and null values a symmetrical distribution (Figure 2A). Kurtosis only takes positive values. Normal distributions have a kurtosis value of 3 and are referred to as mesokurtic distributions. Distributions with a kurtosis below 3 are platykurtic (thin tailed), whereas distribution with a kurtosis above 3 are leptokurtic (heavy tailed) (Figure 2B). The Gini coefficient measures the inequality of a distribution<sup>49,50</sup> and takes values ranging between 0 (representing total equality) and 1 (representing total inequality). It is calculated as the area between the line of equality and the Lorenz curve divided by the total area under the line of equality (Figure 2C). To increase the estimation accuracy of these three parameters, for this analysis we only considered mice with at least 20 simultaneously recorded single units ( $n = 195$  out of 278 mice).

When combining data from the PFC and OB, contrary to the prediction of the blank-slate model, neither the skewness nor

the kurtosis of firing rates (age coefficient = −0.06 and −0.02, CI [−0.19; 0.07] and [−0.05; 0.02],  $p = 0.39$  and  $p = 0.45$ , for skewness and kurtosis, respectively, linear model) and STTC (age coefficient = 0.06 and 0.01, CI [−0.27; 0.39] and [−0.05; 0.07],  $p = 0.73$  and  $p = 0.71$ , for skewness and kurtosis, respectively, linear model) exhibited an age-dependent trend (Figures 2D and 2E). Pooling together firing rate and STTC distributions, 100% of the distributions were right skewed (390 out of 390, skewness >0), and 94% were leptokurtic or heavy tailed (366 out of 390, kurtosis >3). Along the same lines, the Gini coefficient of firing rate did not significantly change over the first two postnatal weeks (age coefficient = −0.004, CI [−0.014; 0.007],  $p = 0.50$ , linear model), whereas the Gini coefficient of STTC even slightly decreased over age (age coefficient = −0.02, CI [−0.03; −0.002],  $p = 0.02$ , linear model) (Figure 2F). This dynamic was consistent across brain regions (Figures S2A–S2C) and robust to changes in the minimum number of single units used as cutoff for analysis (Figure S2D). Even analyzing the distributions of firing rate and STTC after pooling together units recorded in the same brain region and in mice of the same age did not lead to age dependency for any of the evaluated parameters (Figure S3).

These data indicate that, irrespective of brain region, the skewness, tailedness, and inequality of first- and second-order SUA statistics do not increase with age, as would be predicted by the blank-slate model. On the contrary, the only parameter to exhibit a significant age dependence is the Gini coefficient of STTC, which decreases with age. However, this effect is of modest size, and it is the only result that depends on the number of units used as cutoff for a mouse to be included in the analysis (Figure S3D). Further, almost the totality of these distributions is right skewed and heavy tailed. The fact that these results are largely brain region independent indicates that the different developmental speed of the early-maturing OB and the late-maturing PFC does not affect these dynamics. Considering the large size of the investigated datasets, it is also unlikely that we were unable to detect the presence of developmental trends due to a lack of statistical power.

Lastly, solely skewness and kurtosis of both firing rate and STTC robustly correlated with each other ( $r^2 = 0.9$  and 0.88, respectively). Despite similar developmental trajectories, the other pairwise parameter combinations were poorly predictive of each other (median  $r^2 = 0.03$ ) (Figure S4), indicating that they quantify distinct distributions that are largely independent of each other and, thus, not redundant.

### Complex functional network properties of the PFC do not vary over development

Even if the skewness, tailedness, and inequality of firing rate and STTC are largely constant over age, we hypothesized that developmental changes might be detectable at a network level. To test this hypothesis, we resorted to complex network analysis<sup>51</sup> and investigated the functional network topology of the developing PFC *in vivo* (Figure 3A), similarly to what was previously done *in vitro*.<sup>52</sup> To minimize a potential estimation bias due to low number of single units, an inherent drawback of recordings in neonatal mice, we limited this analysis to mice having at least 20 single units ( $n = 108$  out of 131 PFC recordings). We restricted

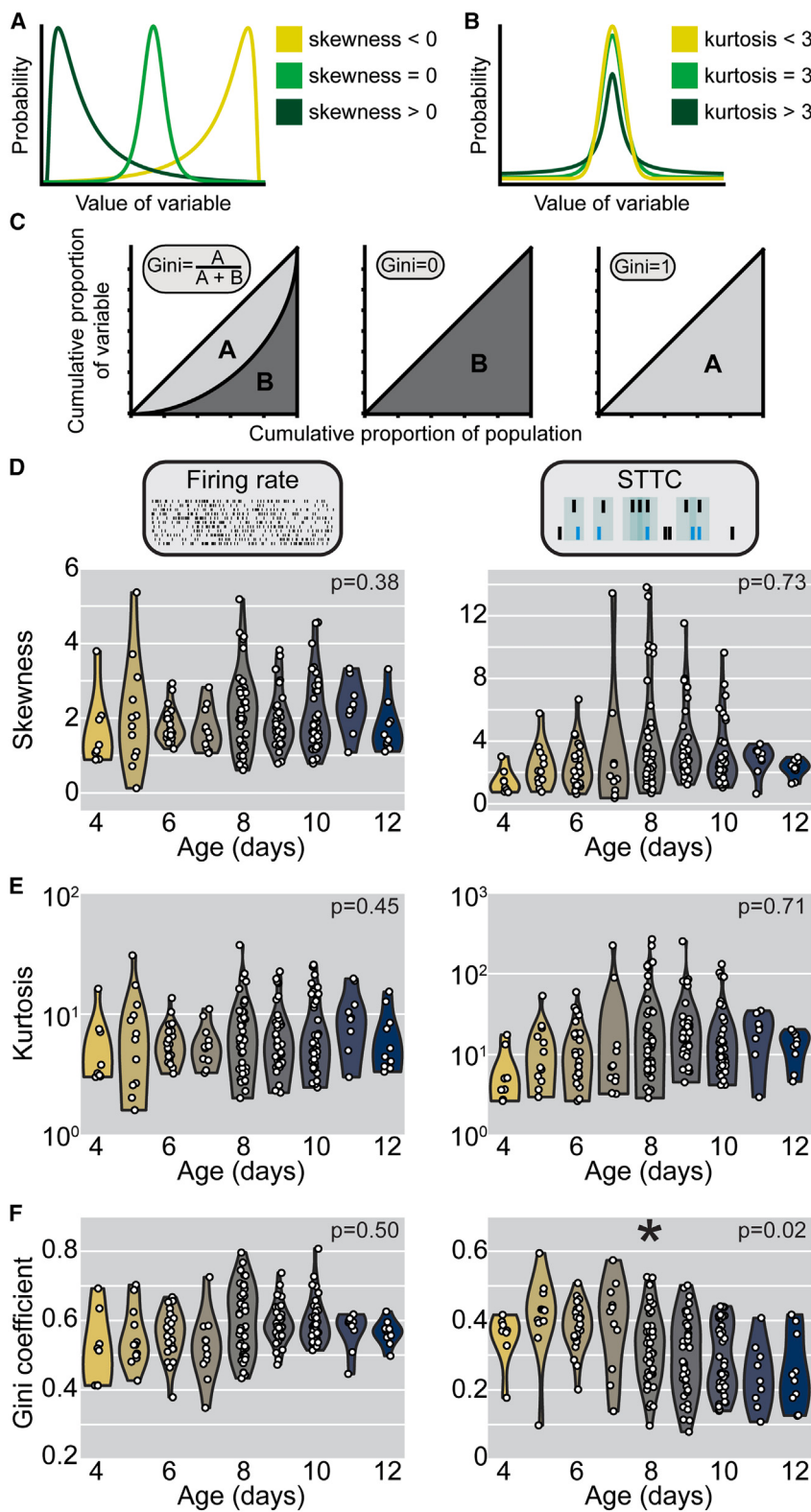


**Figure 2. Skewness, kurtosis, and Gini coefficient of firing rate and STTC over the first two postnatal weeks**

(A) Schematic representation of three distributions with different skewness values.  
 (B) Same as (A) for kurtosis.  
 (C) Lorenz curves for three distributions with different Gini coefficient values and schematic representation of how the Gini coefficient is calculated.  
 (D) Violin plot displaying the skewness of firing rate (left) and STTC (right) of P4–12 mice ( $n = 195$  mice). Color codes for age with 1-day increments.  
 (E and F) Same as (D) for kurtosis (E) and Gini coefficient (F). White dots indicate individual mice, and the shaded area represents the probability density of the variable. Asterisk in (F) indicates a significant effect of age.  $*p < 0.05$ , linear model.  $p$  values in (D)–(F) refer to the effect of age, linear models.

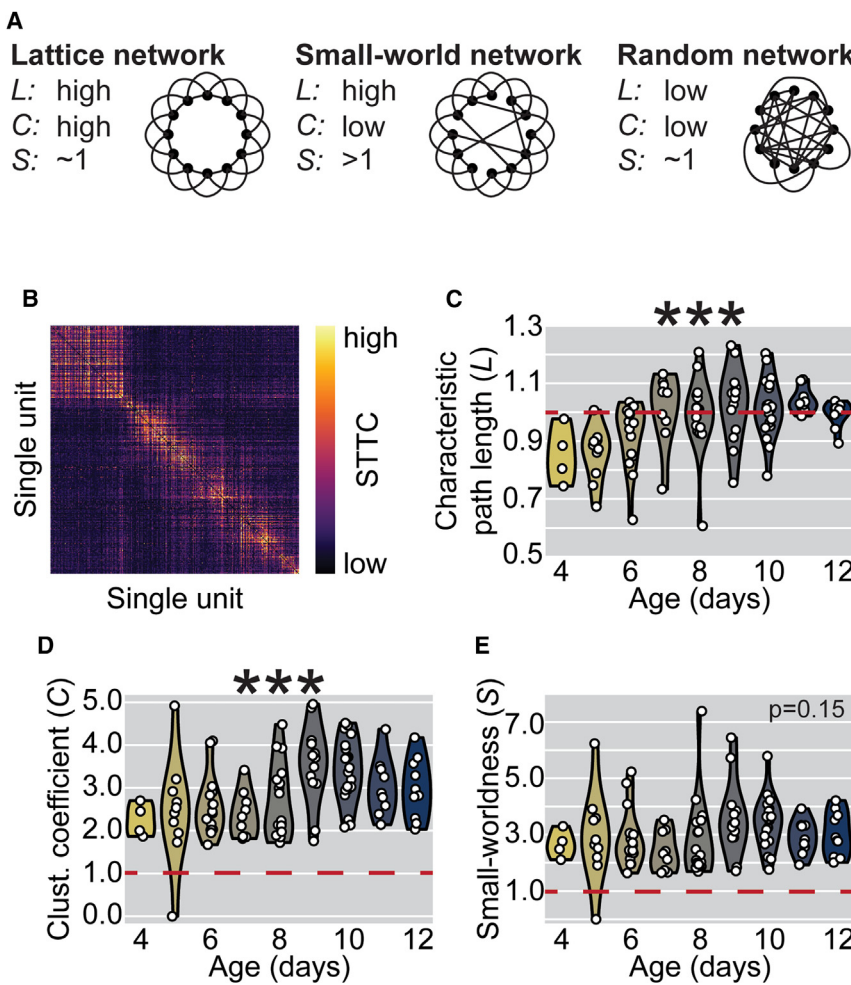


**Figure 3. Complex network analysis in the PFC across the first two postnatal weeks**

(A) Schematic representation of a lattice, small world, and random network and their respective values of characteristic path length (L), clustering coefficient (C), and small-worldness (S).

(B) Weighted adjacency STTC matrix of a representative P10 mouse. Color codes for STTC value. Units are sorted by recording depth.

(C) Violin plot displaying the characteristic path length as a function of age ( $n = 108$  mice). The dashed red line indicates the value of the corresponding random network. Color codes for age with 1-day increments.

(D and E) Same as (C) for clustering coefficient (D) and small-worldness (E). In (C)–(E), white dots indicate individual mice and shaded area represents the probability density of the variable. Asterisks in (C) and (D) indicate a significant effect of age.

\*\*\* $p < 0.001$ , linear models.  $p$  value in (E) refers to the effect of age, linear model.

the investigation to the PFC because the network analysis for OB was biased by the low number of units and the level of recurrent connectivity.

The functional network analysis was carried out on symmetric STTC matrices computed on individual mice, where each node corresponds to a single unit (Figure 3B). These matrices were thresholded and binarized by a shuffling procedure that swapped the identity of the neurons while preserving the population firing rate (see STAR Methods for details). To evaluate the topology of the graphs, we computed their density and three main network properties: characteristic path length (L), clustering coefficient (C), and small-worldness (S) (Figure 3A). These last three parameters were normalized by dividing them with a corresponding null value extracted from random networks with the same density (the dashed red line in Figures 3C–3E indicates the value of the corresponding random network).

Similar to the parameters based on SUA statistics, the density of the graphs did not significantly vary over age (age coefficient =  $-0.003$ , CI  $[-0.009; 0.002]$ ,  $p = 0.23$ , linear model) (Figure S5A). While L values were similar to those computed on random networks (58 out of 108 = 54% networks with normalized L > 1) (Figure 3C), all but one network had larger C values than the corre-

sponding random network (107 out of 108 = 99% networks with normalized C > 1) (Figure 3D). The graphs' transitivity, a parameter that is closely related to the clustering coefficient, was analogously higher than in random networks (107 out of 108 = 99% networks with normalized transitivity > 1) (Figure S5B).

Low L and high C values are typical of so-called small-world networks, a category that includes many real-world networks, including the adult brain<sup>53–55</sup> (but see Hilgetag and Goulas<sup>56</sup>). Accordingly, the small-worldness of the developing PFC was robustly higher than its corre-

spending null value (107 out of 108 = 108 = 99% networks with normalized S > 1) (Figure 3E). The normalized L and C increased over age (age coefficient =  $0.13$  and  $0.02$ , CI  $[0.06; 0.21]$  and  $[0.01; 0.03]$ ,  $p < 10^{-4}$  and  $p < 10^{-4}$ , for normalized L and C, respectively, linear model) (Figures 3C and 3D). While this effect could be explained by an increase on the graph's size (the number of units per mouse),<sup>57</sup> more central for the aim of the project is the fact the normalized S did not vary with age (age coefficient =  $0.07$ , CI  $[-0.02; 0.16]$ ,  $p = 0.15$ , linear model) (Figure 3E). Further, all these results were robust to changes in the minimum number of single units used as cutoff for analysis (Figure S5C).

Thus, complex network analysis revealed that, already during the first two postnatal weeks, the PFC displays a non-random and small-world functional network architecture that is similar to that described in the adult brain<sup>53–55</sup> and is stable over age.

#### The developing brain is in an oligarchical state

Next, we investigated whether the SUA statistics are not only extremely distributed but also correlated to each other. For this, we used multivariate linear regression with age as a covariate, and we evaluated the relationship between the log-transformed firing rate of a neuron and its log-transformed

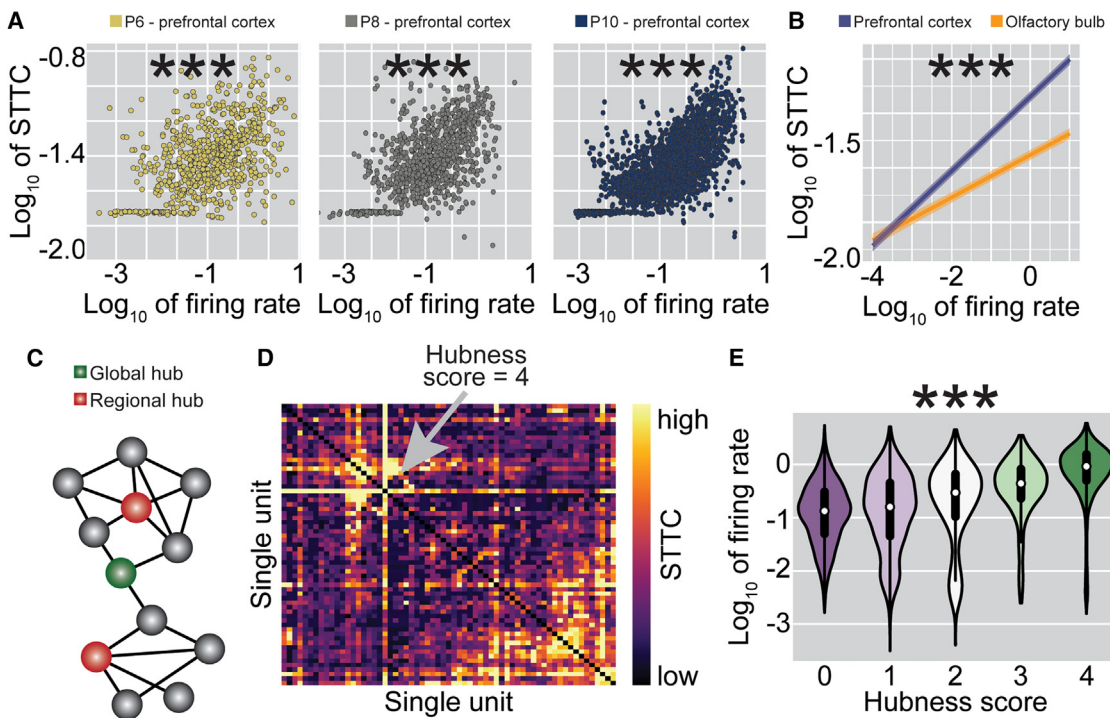


**Figure 4. Firing rate correlates with average STTC and hubness score**

(A) Scatterplot displaying the log-transformed average STTC of prefrontal neurons as a function of their log-transformed firing rate in all recorded P6 (left), P8 (center), and P10 (right) mice. Color codes for age.

(B) Line plot displaying the log-transformed average STTC as a function of log-transformed firing rate across brain regions ( $n = 259$  mice and 14,043 single units). Color codes for brain region.

(C) Schematic representation of a network's graph in which regional (red) and global (green) hubs are highlighted.

(D) Weighted adjacency STTC matrix recorded from the PFC of a P10 mouse. The gray arrow indicates a neuron with high hubness score. Color codes for STTC value.

(E) Violin plot displaying the log-transformed firing rate of a neuron as a function of its hubness score. Color codes for hubness score. In (A), colored dots indicate individual neurons. In (E), data are presented as median, 25<sup>th</sup> percentile, 75<sup>th</sup> percentile, and interquartile range, and the shaded area represents the probability density of the variable. Asterisks in (A) and (B) indicate a significant effect of firing rate and in (E) of hubness score. \*\*\* $p < 0.001$ , linear mixed-effect models.

average STTC. We found that, irrespective of brain region, the two variables robustly correlated with each other (firing rate coefficient = 0.08, CI [0.07; 0.08],  $p < 10^{-70}$ , linear mixed-effect model) (Figures 4A, 4B, and S5D). This correlation between firing rate and average STTC was lower in the OB than in the PFC (firing rate and brain area interaction coefficient = 0.06, CI [0.05; 0.06],  $p < 10^{-84}$ , linear mixed-effect model) (Figure 4B). Since the STTC lacks a firing rate bias,<sup>41</sup> this is indicative of a genuine correlation between the two variables. Consequently, neurons with high firing rates disproportionately contribute to network dynamics during development, a property reminiscent of hub neurons, as recently shown in the developing barrel cortex.<sup>58</sup> We define this state, in which extreme distributions are tightly correlated with each other, as being “oligarchical.”

To investigate whether the firing rate of a neuron also correlates to its network-level features, we used the prefrontal STTC matrices described in the paragraph above and extracted four different regional and global “hubness” metrics for each individual node: degree (i.e., total number of connections), strength (i.e., sum of connection weights), betweenness centrality (the

fraction of shortest paths containing a given node), and closeness centrality (the reciprocal of the average shortest path for a given node) (Figures 4C and 4D). For each of these measures, we then assigned a score of 0 or 1 to each node, depending on whether it exceeded the 75<sup>th</sup> percentile of that specific metric.<sup>52</sup> Summing the individual scores, we obtained a composite hubness score, with values ranging from 0 to 4. The majority of neurons (6,580 out of 10,512 = 63%) had a hubness score of 0, whereas a smaller proportion (1,471 out of 10,512 = 14%) of neurons received a hubness score of 4. As previously reported in 2D neuronal cultures,<sup>52</sup> the hubness score robustly correlated with firing rate (hubness score effect,  $p < 10^{-70}$ , linear mixed-effect model), with the median firing rate differing by almost an order of magnitude between neurons with hubness score 0 and 4 (Figure 5E).

These data indicate that the developing cortex is not only an environment characterized by stably extreme SUA statistics distributions but also that it exhibits a peculiar oligarchical state, in which the firing rate of a neuron robustly correlates with the strength of its pairwise interactions and its network-level properties.

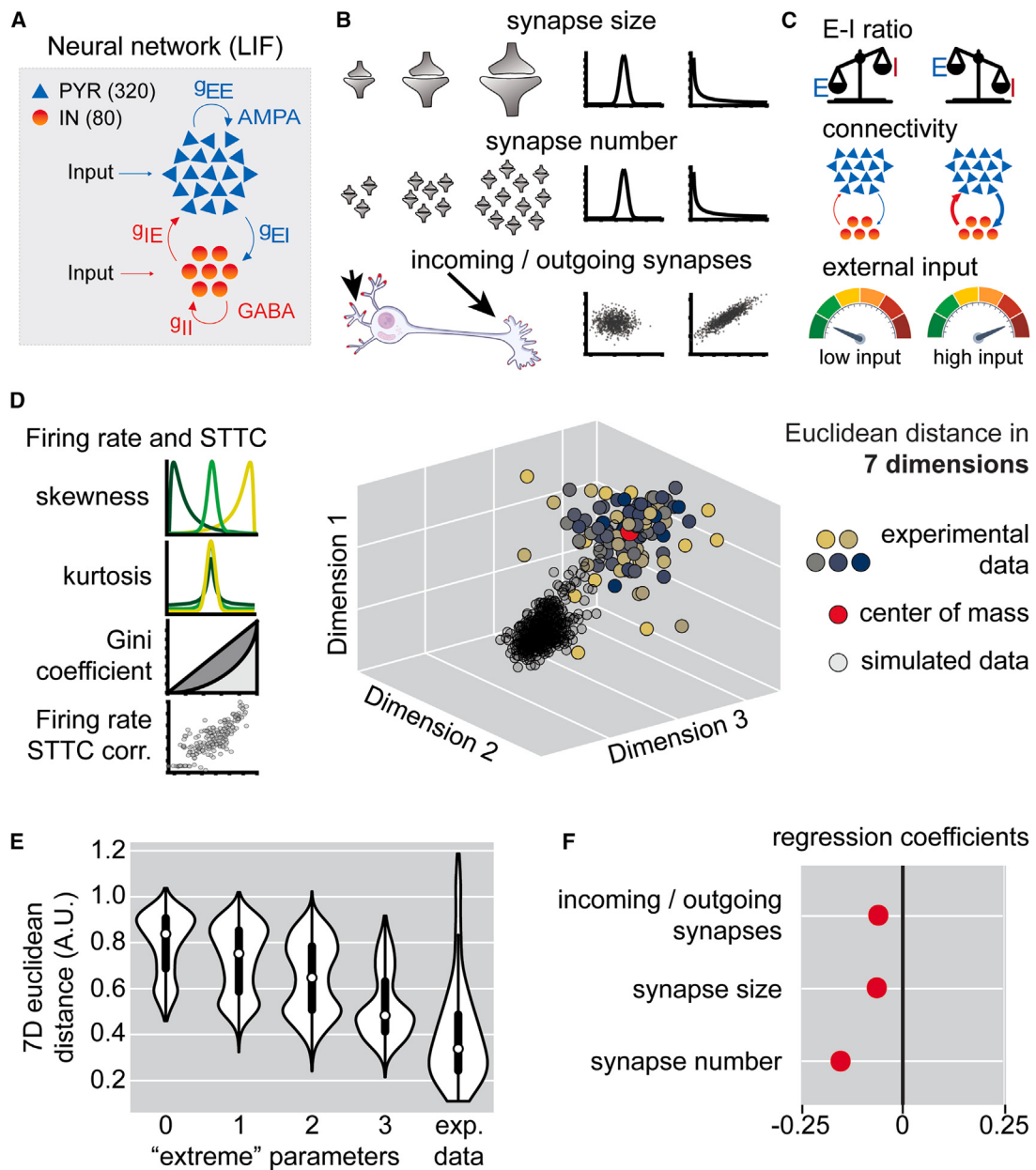


**Figure 5. Spiking neural network modeling of the distribution shape of SUA statistics in the developing PFC**

(A) Schematic representation of the neural network model.

(B and C) Same as (A) for the three synaptic parameters (B) and the simulation parameters that were treated as random variables (C).

(D) Schematic representation of the parameters that were used to evaluate the distribution shape of the experimental and simulated spiking data (left) and the approach that was used to evaluate the distance between experimental and simulated data (right). Note that the plot is for visualization purposes only. Even though only three dimensions are shown, the distance between simulated and experimental data were calculated in a seven-dimensional space. Color in the scatterplot codes for age.

(E) Violin plot displaying the distance between simulated data and the center of mass of experimental data as a function of the number of synaptic parameters set in their "extreme" configuration.

(F) Multivariate regression coefficients for the three synaptic parameters over the distance from the center of mass of experimental data. In (E), data are presented as median, 25<sup>th</sup> percentile, 75<sup>th</sup> percentile, and interquartile range, and the shaded area represents the probability density of the variable. In (F), regression coefficients are presented as mean and 95% CI.

### Extreme synaptic distributions are necessary to recapitulate early PFC activity in a spiking neural network model

We hypothesized that, to generate such extreme distributions of the SUA statistics, analogously extremely distributed structural synaptic parameters are necessary. To explore this proposition, we simulated ~8,000 spiking neural networks of interconnected conductance-based leaky integrate-and-fire (LIF) neurons. The networks mimicked spontaneous activity: they did not receive any structured input and did not perform any task. The simulated networks had no spatial structure and consisted of 400 neurons, 80% of which were excitatory (PYRs) and 20% inhibitory (INs), in line with anatomical data for neocortical areas.<sup>59,60</sup> PYRs were simulated with outgoing excitatory AMPA synapses, while INs were equipped with outgoing inhibitory GABAergic synapses (Figure 5A). In these models, we investigated how the simulated firing statistics were affected by three structural (synaptic) parameters: (1) whether the size of synapses followed a normal or a log-normal distribution, (2) whether the number of synapses of individual neurons followed a normal or a log-normal distribution, and (3) whether the number of dendritic and axonic (incoming and outgoing) synapses were correlated or uncorrelated with each other (Figure 5B). This resulted in a total of  $2^3 = 8$  possible synaptic parameters combinations. To avoid choosing an arbitrary structural network architecture to test the effect of these three variables, a set of other parameters (average size of AMPA and GABA synapses, average connectivity, and the strength of the noisy input driving PYRs and INs) were randomly drawn from a range of biologically constrained values (see STAR Methods for details) (Figure 5C). Given that the general structural network architecture is inspired by the neocortical anatomical organization (e.g., average connectivity and proportion of PYRs and INs), the simulated data were compared to PFC recordings.

To evaluate how accurately the different structural network architectures recapitulated the SUA statistics of the developing PFC, we employed the same parameters that we used to describe the experimental data. For each simulation, we computed the simulated firing rates and STTC, and, for both variables, we extracted their skewness, kurtosis, Gini coefficient, and the correlation between log-transformed firing rates and average STTC. We then derived the coordinates of the center of mass of the experimental data in this seven-dimensional parameter space and calculated the Euclidian distance from every simulation (see simplified scheme in Figure 5D).

Using multivariate linear regression, we observed a decrease in the distance from the experimental data's center of mass as a function of the number of structural parameters set in its extreme configuration (log-normal distribution of synapse size and number, and correlated number of incoming and outgoing synapses) (Figure 5E). Further, the distance from the experimental center of mass decreased supra-linearly as a function of the number of extreme parameters (0–1 extreme parameters distance difference = 0.07, 1–2 extreme parameters distance difference = 0.09, 2–3 extreme parameters distance difference = 0.12, linear model) (Figure 5E).

This effect is also visually appreciable when the seven dimensions in which we evaluated the model fit are reduced using t-distributed stochastic neighborhood embedding (tSNE) (Figure S6A). When few synaptic parameters are set to their extreme configuration, there is little to no overlap between experimental and simulated data. Conversely, when all three synaptic parameters are set to their extreme configuration, the areas of maximum density of the two distributions are overlapping (Figure S6A).

Taken individually, the structural parameter with the largest effect on the average distance from the experimental data's center of mass was the distribution of synapse number (regression coefficient =  $-0.16$ , linear model), followed by the distribution of synaptic weight (regression coefficient =  $-0.06$ , linear model) and by the proportionality of incoming and outgoing synapses (regression coefficient =  $-0.06$ , linear model) (Figure 5F). Next, we considered the effect of the three synaptic parameters on individual properties of the simulated SUA statistics (Figures S6B–S6H). We found that the distribution of the synapse number had the largest effect on (1 and 2) skewness of firing rate and STTC, (3) the kurtosis of STTC, (4) the Gini coefficient of firing rate and (5) the log-log correlation between firing rate and average STTC. The proportionality of incoming and outgoing synapses had the largest effect on (1) the kurtosis of firing rate and (2) the Gini coefficient of STTC. The distribution of synaptic weights did not have the largest effect on any of the seven parameters (Figures S6B–S6H). Lastly, we run a separate set of simulation varying network size and found that it only minimally affected the distance between simulated and experimental data (Figure S6J).

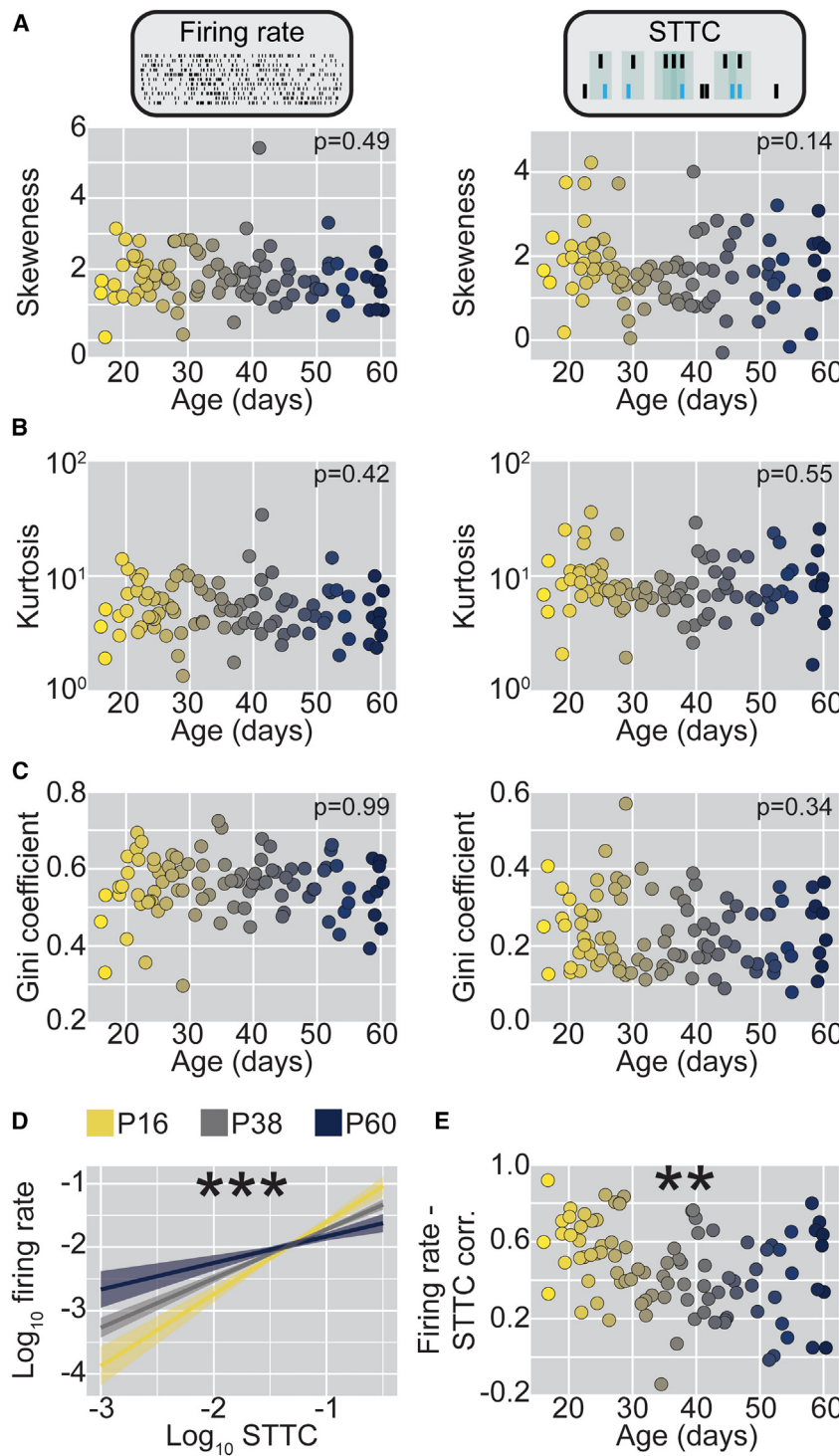
Taken together, these data indicate that, in spiking neural networks simulations, extreme distributions of synaptic parameters are required to stably recapitulate the SUA statistics that we observed in the developing PFC. The distribution of synapse number on individual neurons is the synaptic parameter with the largest influence on the model fit. However, all three synaptic parameters play a significant role and influence different aspects of the simulated data.

### The shape of the SUA statistics distributions is stable throughout adulthood, while the oligarchy decreases with age

So far, we have shown that, already shortly after birth, the brain has a right-skewed, heavy-tailed, and unequal distribution of SUA statistics that largely does not vary during the first two postnatal weeks. Since similar properties have been previously reported for the adult brain, the question arises of whether and how the extremeness of these parameters varies throughout late development and into adulthood. To address this question, we chronically recorded from the PFC of head-fixed mice from P16 to P60 ( $n = 24$  mice, 95 recordings, 2,498 single units, and 36,899 spike train pairs).

SUA firing rate and STTC did not vary with age (age coefficient =  $-0.003$  and  $-10^{-4}$ , CI  $[-0.003; 0.001]$  and  $[-6 \times 10^{-4}; 4 \times 10^{-4}]$ ,  $p = 0.28$  and  $p = 0.63$ , respectively, generalized linear mixed-effect model) (Figures S7A and S7B).

Analogously to the data for the neonatal brain, the skewness of the SUA statistics did not change also for the P16–60



developmental time window (age coefficient =  $-0.004$  and  $-0.01$ , CI  $[-0.02; 0.007]$  and  $[-0.02; 0.003]$ ,  $p = 0.49$  and  $p = 0.14$ , for firing rate and STTC, respectively, linear mixed-effect model) (Figure 6A). Along the same line, also the kurtosis (age coefficient =  $-0.001$  and  $-0.001$ , CI  $[-0.005; 0.002]$  and  $[-0.005; 0.002]$ ,  $p = 0.42$  and  $p = 0.55$ , for firing rate and STTC, respec-

**Figure 6. Skewness, kurtosis, Gini coefficient, and correlations of firing rate and STTC in P16–60 mice**

(A) Scatterplot displaying the skewness of firing rate (left) and STTC (right) of P16–60 mice ( $n = 24$  mice and 95 recordings). Color codes for age with 1-day increments.

(B and C) Same as (A) for kurtosis (B) and Gini coefficient (C).

(D) Line plot displaying the log-transformed average STTC as a function of log-transformed firing rate across ages ( $n = 24$  mice and 2,498 single units). Color codes for age.

(E) Same as (A) for the Pearson correlation between log-transformed average STTC and log-transformed firing rate within individual mice. In (A–C) and (E), colored dots indicate individual recordings. In (D), data are presented as mean and 95% CI. Asterisks in (D) and (E) indicate a significant effect of age.

\*\*\* $p < 0.001$ , \*\* $p < 0.01$ , linear mixed-effect models.

$p$  values in (A)–(C) refer to the effect of age, linear mixed-effect models.

tively, linear mixed-effect model) and the Gini coefficient (age coefficient =  $10^{-5}$  and  $7 \times 10^{-4}$ , CI  $[-0.001; 0.001]$  and  $[-0.002; 8 \times 10^{-4}]$ ,  $p = 0.99$  and  $p = 0.34$ , for firing rate and STTC, respectively, linear mixed-effect model) of the two variables remained constant for the investigated time window (Figures 6B and 6C).

Similar to what reported for early development, also in the adult PFC the log-transformed firing rate of a neuron and its average STTC strongly correlated with each other (average STTC coefficient =  $1.53$ , CI  $[1.34; 1.71]$ ,  $p < 10^{-56}$ , linear mixed-effect model) (Figure 6D). However, fitting a model that included an interaction of STTC with age revealed that the correlation strength between the two variables decreased over late development (age and average STTC interaction coefficient =  $-0.03$ , CI  $[-0.05; -0.02]$ ,  $p < 10^{-5}$ , linear mixed-effect model) (Figure 6D). Accordingly, the Pearson correlation between firing rate and average STTC on an individual-mouse basis robustly declined with age, from roughly  $\sim 0.6$  to  $\sim 0.3$  (age coefficient =  $-0.006$ , CI  $[-0.009; -0.002]$ ,  $p = 0.001$ , linear mixed-effect model) (Figure 6E).

Thus, in the mouse PFC, the extremeness of SUA statistics distributions does not significantly change between P16 and P60. However, the correlation between firing rate and STTC is roughly halved from P16 to P60, indicating that the oligarchical state in PFC is more pronounced during early development than at adulthood.

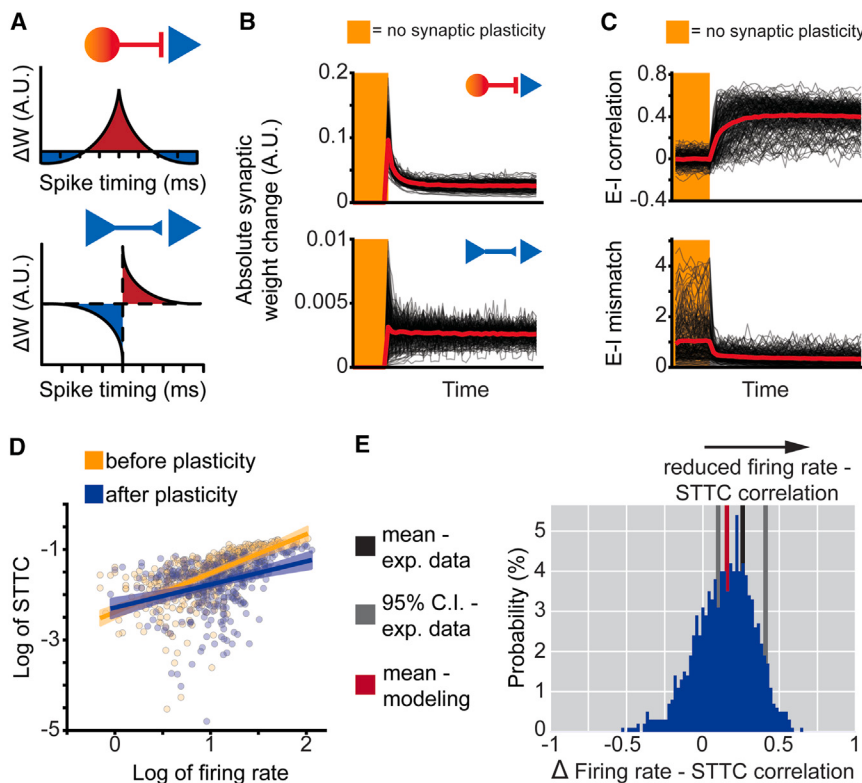


**Figure 7. Spike-time-dependent inhibitory synaptic plasticity decreases the correlation between firing rate and STTC**

(A) Schematic representation of the simulated inhibitory (top) and excitatory (bottom) synaptic plasticity rules.

(B) Line plot of the IN-PYR (top) and PYR-PYR (bottom) synaptic weight changes over time. The shaded area indicates the period without synaptic plasticity.

(C) Line plot of excitatory and inhibitory currents correlation (top) and absolute difference (bottom) over time. The shaded area indicates the period without synaptic plasticity.

(D) Scatter and line plot of a representative example of the correlation between simulated firing rate and average STTC before (yellow) and after (blue) synaptic plasticity.

(E) Histogram plot of the difference in simulated firing rate and average STTC correlation before and after synaptic plasticity. The black line indicates the mean of the experimental data, the two gray lines the 95% CI of the mean, and the red line the mean of the simulated data. In (B) and (C), individual black lines represent individual simulations and the red line represents the mean across simulations. For visualization purposes, only one-fifth of the individual simulations are shown. In (D), individual dots represent individual simulated neurons, and data are presented as mean and 95% CI.

### Inhibitory synaptic plasticity parsimoniously explains the gradual disappearance of the oligarchy

Throughout the same developmental phase during which we observed a decrease in the correlation between the firing rate of a neuron and its average STTC, the cortex transitions into a state of detailed E-I balance,<sup>61</sup> a phenomenon that has been linked to inhibitory synaptic plasticity.<sup>62</sup> Given the critical role that E-I ratio plays in controlling correlations among neurons,<sup>39</sup> we hypothesized that this transition might explain the progressive decline of the correlation between firing rate and STTC.

To test this hypothesis, we resorted to spiking neural network modeling with an architecture analogous to the one used to model early cortical activity. After an initial period in which the networks were run with frozen synaptic sizes and all the synaptic parameters in their extreme configuration, we added symmetric spike-time-dependent inhibitory plasticity (ISTDP) on the synapses connecting INs to PYRs<sup>62</sup> (Equation 1) and classic asymmetric Hebbian plasticity (STDP) on PYR-PYR excitatory synapses<sup>63</sup> (Figure 7A). The original formulation of the ISTDP rule implemented a single target firing rate ( $\alpha$ , Equation 1) for the entire population of PYRs. In this study, we instead decided to draw  $\alpha$  from a log-normal distribution to better recapitulate the diversity of the experimentally observed firing rates (see STAR Methods for details):

$$\frac{dW}{dt} = \frac{\eta(\text{pre} * \text{post} - \alpha * \text{pre})}{\tau_{\text{STDP}}} \quad (\text{Equation 1})$$

where  $W$  is an IN-PYR synaptic weight,  $\text{pre}$  and  $\text{post}$  are the pre- and post-synaptic activity,  $\alpha$  is the target rate for the post-synaptic PYR and is drawn from a log-normal distribution,  $\tau_{\text{STDP}}$  is the decay time constant of the plasticity rule, and  $\eta$  is the learning rate.

Analogously to the approach that we previously described, also for this set of simulations, we treated several other structural parameters as random variables, and we systematically varied them within the same biologically constrained range of values that we employed for the former simulations. To evaluate the effect of synaptic plasticity, we compared the SUA statistics of the frozen synapses phase and those of the last fifth of the simulated data, a phase in which synaptic changes were stable (Figure 7B).

Analogously to previous results,<sup>62</sup> we observed that adding ISTDP resulted in a network with detailed E-I balance. ISTDP increased the correlation between incoming excitatory and inhibitory currents across neurons (Figure 7C, top) and reduced the temporal mismatch (i.e., the absolute value of the difference) between excitatory and inhibitory currents across time (computed in 5-s bins) within individual neurons (Figure 7C, bottom).

In line with our hypothesis, we found that adding ISTDP and STDP to the network also decreased the correlation between firing rate and average STTC, similarly to what we experimentally observed in P16–60 mice (mean decrease in firing rate – average STTC correlation in simulated data = 0.16, in experimental data = 0.26, CI [0.11; 0.41], Figures 7D and 7E). When we further evaluated the effects of synaptic plasticity, we found that it only

minimally affected the skewness, kurtosis, and Gini coefficient of firing rate and STTC, in line with the experimental data from the PFC of P16–60 mice (Figure S7). Of these six parameters, only the kurtosis and the Gini coefficient of firing rate were narrowly outside the 95% CI of the experimental values (Figures S7C–S7H).

To investigate the differential role of ISTDp and STDP in decreasing the correlation between firing rate and average STTC, we next run two sets of simulations with only one of the two synaptic plasticity rules. These simulations revealed that, while ISTDp-only networks displayed a decrease between firing rate and average STTC that was comparable to networks with both synaptic plasticity rules, the correlation between the two variables was unchanged in STDP-only networks (Figure S7I). However, ISTDp-only simulations provided an overall significantly worse fit to the experimental data than networks with both synaptic plasticity rules (Figure S7J). Thus, the two synaptic plasticity rules have different effects on the simulated spiking activity. ISTDp is mainly responsible for the decrease in the oligarchical organization, whereas STDP allows this to happen while only minimally affecting the skewness, kurtosis, and Gini coefficient of firing rate and STTC.

Taken together, these data indicate that adding ISTDp and STDP to a spiking neural network parsimoniously recapitulates the developmental decrease in the correlation between firing rate and STTC while only minimally affecting the distribution shape of the two variables, consistent with what we observed in the PFC of P16–60 mice.

## DISCUSSION

A fascinating property of the adult brain is that a large number of parameters, ranging from the size of synapses to the power of extracellular currents,<sup>1,3,4</sup> follow extreme distributions. This organization has been suggested to have many desirable properties,<sup>10,27</sup> but how and when it arises is still a matter of debate. Here, we report that, in the PFC and OB, two brain regions exemplifying slow and fast maturational dynamics, in the first days of extrauterine life, the distributions of first- and second-order SUA statistics are already extreme: right skewed, heavy tailed, and highly unequal. While the central tendency of these distributions varies across development, their shape remains largely unchanged until adulthood. We also show that early brain activity is in an oligarchical state in which high-firing-rate neurons display hub-like properties and exert a disproportionate influence on their local network, a phenomenon that becomes less prominent as mice age. Leveraging spiking neural network modeling, we demonstrate that, to recapitulate these network properties, analogously extremely distributed synaptic parameters are needed. We conclude by showing that the progressive disappearance of the oligarchical state can be parsimoniously explained by introducing an inhibitory synaptic plasticity rule that establishes a detailed excitation-inhibition balance. This work suggests that the distribution shape of structural and functional neural parameters is not fundamentally altered by developmental processes but rather is preconfigured and experience independent.

In altricial animals such as rodents, the first postnatal week roughly corresponds to mid-late gestation in humans.<sup>38</sup> At this early stage, brain activity has several unique traits, such as discontinuity,<sup>38</sup> highly correlated spiking activity,<sup>39,47,48</sup> the presence of transient cell types and circuits,<sup>64</sup> extremely low firing rates,<sup>39,65</sup> low levels of inhibition,<sup>39,66,67</sup> and a loose temporal coordination of excitation and inhibition.<sup>61,62</sup> Importantly, sensory systems are still very underdeveloped. In rodents, the retina becomes light sensitive around P8–P9,<sup>65,68</sup> and eye opening only takes place around P14–P15, a few days after hearing onset occurs.<sup>69</sup> The whisking-related sensory system also follows a similar timeline. In the first postnatal week, ~90% of whisker movements do not induce increased firing rate in the somatosensory cortex, and ~90% of firing in the somatosensory cortex is unrelated to whisker movements.<sup>70</sup> Even after splitting whisker movements by size and only considering the few large ones that occur, the somatosensory cortex is active concomitantly with a whisker movement less than 50% of the time.<sup>71</sup> Whisker-elicited sensory responses are initially mainly the result of passive stimulations by the dam and the littermates, while robust active whisking only emerges around P10–P12.<sup>72–74</sup> Solely the olfactory system follows a distinct developmental dynamic and, even though it is also still developing,<sup>75</sup> it is already functional and behaviorally relevant in the first postnatal days.<sup>36,37</sup> Despite the paucity of sensory information that is therefore available in the first postnatal week, we find that the distribution of SUA statistics is already extreme and does not significantly vary from early development to adulthood. Corroborating the idea that experience does not play a significant role in this process, we find no differences between the OB, which is already “online,” and the PFC, which is supposed to be one of the slowest-developing brain regions.<sup>38</sup> We further show that, already from P4 onwards, the PFC also displays a complex network topology that is reminiscent of small-world networks, a property that is typical of many real-world networks,<sup>76</sup> including the adult brain<sup>53–55</sup> (but see Hilgetag and Goulas<sup>56</sup>).

These results are difficult to reconcile with the hypothesis that brain structure is initially “diffuse” and only later acquires the structural organization that is typical of the adult brain.<sup>30,31,77</sup> Rather, they support several recent studies that have highlighted the importance of “nature over nurture”<sup>78,79</sup> in establishing neural circuits and the distributions of their parameters. For instance, in neuronal cultures, the variance of glutamatergic synaptic sizes does not differ between networks that are silenced from plating onwards and networks that are spontaneously active.<sup>7</sup> Similarly, cultures of dissociated neurons exhibit the ability to self-organize into a complex network topology with small-world properties that are characterized by extreme distributions of firing rates and connection weights.<sup>52</sup> Extreme distributions of firing rates and functional connectivity are also observed in human brain organoids,<sup>80–82</sup> which, despite not having access to sensory inputs, even display structured spiking “protosequences.”<sup>82</sup> Along the same lines, *in vivo* blocking of synaptic transmission in the mouse hippocampus does not alter the distribution of spine sizes,<sup>83</sup> and “soloist” neurons (uncorrelated to the overall local firing) coexist with “choristers” (strongly correlated with local firing) already in the first postnatal week.<sup>84</sup> Even more surprisingly, completely abolishing all central nervous system

activity for the first 4 days of life of the larval zebrafish only minimally affects the tuning and functionality of neurons and the ability of the fish to learn a complex visuomotor task.<sup>78</sup> Intriguingly, similar concepts are beginning to percolate also in the field of artificial intelligence,<sup>85</sup> which has traditionally been dominated by a bottom-up and learning-based approach.

The relationship between the firing rate of a neuron and the strength of its pairwise interactions with other neurons is complex and still debated. A number of experimental and theoretical studies found a positive correlation between the two variables.<sup>86–89</sup> However, this relationship has also been reported to be absent or even negative.<sup>90–93</sup> Here we show that, in the PFC and OB of P4–12 mice, there is a strong positive correlation between firing rate and average pairwise interaction of a neuron, as measured by the STTC coefficient. Thus, neurons with extreme firing rates are also likely to have extreme average STTC values, an organization that we refer to as oligarchical. The correlation between firing rate and STTC weakens throughout development, but it is present also in adulthood. In the early PFC, firing rate also correlates with a neuron's hubness score, a composite metric that encompasses four different measures of local and global hubness. The topic of hub neurons, defined as a subclass of neurons that has an outsized influence on the network activity, has been the subject of extensive experimental and theoretical research in the developing brain.<sup>58,94–96</sup> In agreement with our results, hub neurons in the developing entorhinal<sup>94,95</sup> and barrel cortex<sup>58</sup> are also characterized by high firing rates and high functional connectivity, a prediction that is shared by theoretical work.<sup>97</sup> Previous work has also shown that hub neurons are generally INs, something that we could not investigate in the current study due to the difficulty of separating INs and PYRs based on their waveform properties in the early developing brain.<sup>98</sup> This work further shows that, in a neural network model, adding inhibitory synaptic plasticity results in detailed E-I balance and decreases the influence of high-firing-rate neurons on the network activity. Thus, we propose that the loose temporal E-I balance that is typical of the developing brain<sup>61,62</sup> might be a permissive mechanism for the role exerted by hub neurons on their surroundings. Whether the developmental shift of E-I ratio toward inhibition<sup>39,66</sup> also plays a role remains to be investigated.

Lastly, we show that there is a mechanistic link between the distribution of structural (synaptic) and functional (SUA statistics) parameters. In particular, we report that, in a spiking neural network model, three synaptic parameters have a strong influence on the extremeness of the simulated spiking activity: (1) whether the size of synapses follows a log-normal distribution, (2) whether the number of synapses of individual neurons follows a log-normal distribution, and (3) whether the number of dendritic and axonic (incoming and outgoing) synapses are correlated with each other. The three parameters have a synergistic effect on the model goodness of fit to the experimental data and a distinct impact on different properties (skewness, kurtosis, and Gini coefficient) of the simulated firing rate and STTC distributions. While a large body of evidence supports the notion that the size and number of synapses follow an extreme distribution,<sup>1</sup> to the best of our knowledge, whether the number of dendritic and axonic synapses are correlated with each other has not

been explicitly investigated in mammals. However, a recent study found that, in the mouse PFC, the length of a neuron's dendrite and axon are positively correlated.<sup>99</sup> Further, in a full-brain *Drosophila melanogaster* reconstruction, the numbers of incoming and outgoing synapses are tightly correlated with each other (Person coefficient = 0.8).<sup>100</sup> The fact that extremely distributed synaptic parameters are required to faithfully reproduce the SUA statistics of the developing PFC suggests that the distribution of synaptic parameters is also experience independent.

In summary, we report that the extremeness with which functional and structural parameters are distributed is stable across a large portion of the lifespan, which suggests that the brain is in a preconfigured state and that experience-dependent processes do not fundamentally alter this aspect of its organization. Further elucidating the principles underlying the establishment of neural circuits might prove insightful for advancing the field of biological and artificial intelligence alike.

### Limitations of the study

This study has several limitations. First, despite investigating mice from a very early developmental phase, and doing so also in the PFC, one of the slowest-developing brain regions, we cannot exclude that some experience-dependent processes have not already taken place. Second, we do not directly experimentally probe whether the distribution shape of synaptic parameters is stable across the first postnatal weeks. However, our modeling results generate a number of predictions that could be experimentally addressed: (1) synapse size and number on individual neurons follow extreme distributions already in the first postnatal week, (2) the shape of these distributions should be stable across development, and (3) the number of incoming and outgoing synapses should be tightly correlated. Third, while our results argue against a role of experience in shaping these processes, we do not provide an alternative mechanistic answer to the question. This topic has, however, already been the subject of a number of theoretical studies.<sup>7,9,83,97</sup> Further, we generated a large and detailed experimental open-access database that could be instrumental in benchmarking future research on this topic. An approach that we believe might be of particular interest is that of generative models.<sup>101,102</sup> Illustrating the promise of this approach, generative models solely based on spatiotemporal gradients of neuronal development<sup>103</sup> or homophily principles<sup>81</sup> can recapitulate important features of the complex topology of adult brains.

### STAR★METHODS

Detailed methods are provided in the online version of this paper and include the following:

- [KEY RESOURCES TABLE](#)
- [RESOURCE AVAILABILITY](#)
  - Lead contact
  - Materials availability
  - Data and code availability
- [EXPERIMENTAL MODEL AND STUDY PARTICIPANT DETAILS](#)
- [METHOD DETAILS](#)
  - *In vivo* electrophysiology in P4–12 mice
  - *In vivo* electrophysiology in P16–60 mice

● QUANTIFICATION AND STATISTICAL ANALYSIS

- Spike sorting
- SUA firing statistics and shape distribution parameters
- Complex network properties
- Neural network modeling
- Statistical modeling

**SUPPLEMENTAL INFORMATION**

Supplemental information can be found online at <https://doi.org/10.1016/j.celrep.2024.114267>.

**ACKNOWLEDGMENTS**

We thank Sebastian Bitzenhofer and Irina Pochinok for valuable discussions and feedback on the manuscript and P. Putthoff, A. Marquardt, and A. Dahlmann for excellent technical assistance. This work was funded by grants from the European Research Council (ERC-2015-CoG 681577to I.L.H.-O.), Marie Curie Training Network euSNN (MSCA-ITN-H2020-860563 to I.L.H.-O.), Horizon2020 DEEPER 101016787, the German Research Foundation (437610067, 178316478, and 302153259 to I.L.H.-O.), and Landesforschungsförderung Hamburg (LFF76 and LFF73 to I.L.H.-O.).

**AUTHOR CONTRIBUTIONS**

M.C. and I.L.H.-O. designed the experiments and wrote the manuscript. M.C., J.K.K., M.H., and Y.-N.C. carried out the experiments. M.C. analyzed the experimental data and carried out neural network modeling. All authors interpreted the data and discussed and commented on the manuscript.

**DECLARATION OF INTERESTS**

The authors declare no competing interests.

Received: December 20, 2023

Revised: March 13, 2024

Accepted: May 8, 2024

Published: May 24, 2024

**REFERENCES**

- 1. Buzsáki, G., and Mizuseki, K. (2014). The log-dynamic brain: how skewed distributions affect network operations. *Nat. Rev. Neurosci.* **15**, 264–278.
- 2. Buzsaki, G., and Buzsaki, G. (2021). *The Brain from Inside Out* (Oxford University Press).
- 3. Levenstein, D., and Okun, M. (2023). Logarithmically scaled, gamma distributed neuronal spiking. *J. Physiol.* **601**, 3055–3069.
- 4. Wilting, J., and Priesemann, V. (2019). 25 years of criticality in neuroscience - established results, open controversies, novel concepts. *Curr. Opin. Neurobiol.* **58**, 105–111.
- 5. Barabasi, A.L., and Albert, R. (1999). Emergence of scaling in random networks. *Science* **286**, 509–512.
- 6. Song, S., Sjöström, P.J., Reigl, M., Nelson, S., and Chklovskii, D.B. (2005). Highly nonrandom features of synaptic connectivity in local cortical circuits. *PLoS Biol.* **3**, e68.
- 7. Hazan, L., and Ziv, N.E. (2020). Activity Dependent and Independent Determinants of Synaptic Size Diversity. *J. Neurosci.* **40**, 2828–2848.
- 8. Wittner, L., Henze, D.A., Záboršky, L., and Buzsáki, G. (2007). Three-dimensional reconstruction of the axon arbor of a CA3 pyramidal cell recorded and filled in vivo. *Brain Struct. Funct.* **212**, 75–83.
- 9. Loewenstein, Y., Kuras, A., and Rumpel, S. (2011). Multiplicative Dynamics Underlie the Emergence of the Log-Normal Distribution of Spine Sizes in the Neocortex In Vivo. *J. Neurosci.* **31**, 9481–9488.
- 10. Ikegaya, Y., Sasaki, T., Ishikawa, D., Honma, N., Tao, K., Takahashi, N., Minamisawa, G., Ujita, S., and Matsuki, N. (2013). Interpyramidal spike transmission stabilizes the sparseness of recurrent network activity. *Cereb. Cortex* **1991** **23**, 293–304.
- 11. Keck, T., Keller, G.B., Jacobsen, R.I., Eysel, U.T., Bonhoeffer, T., and Hübener, M. (2013). Synaptic scaling and homeostatic plasticity in the mouse visual cortex in vivo. *Neuron* **80**, 327–334.
- 12. Cossell, L., Iacaruso, M.F., Muir, D.R., Houlton, R., Sader, E.N., Ko, H., Hofer, S.B., and Mrsic-Flogel, T.D. (2015). Functional organization of excitatory synaptic strength in primary visual cortex. *Nature* **518**, 399–403.
- 13. Wang, S.S.-H., Shultz, J.R., Burish, M.J., Harrison, K.H., Hof, P.R., Towns, L.C., Wagers, M.W., and Wyatt, K.D. (2008). Functional trade-offs in white matter axonal scaling. *J. Neurosci.* **28**, 4047–4056.
- 14. Morales-Gregorio, A., van Meegen, A., and van Albada, S.J. (2023). Ubiquitous lognormal distribution of neuron densities in mammalian cerebral cortex. *Cereb. Cortex* **33**, 9439–9449.
- 15. Fujisawa, S., Amarasingham, A., Harrison, M.T., and Buzsáki, G. (2008). Behavior-dependent short-term assembly dynamics in the medial prefrontal cortex. *Nat. Neurosci.* **11**, 823–833.
- 16. Hromádka, T., DeWeese, M.R., and Zador, A.M. (2008). Sparse Representation of Sounds in the Unanesthetized Auditory Cortex. *PLoS Biol.* **6**, e16.
- 17. Mizuseki, K., and Buzsáki, G. (2013). Preconfigured, skewed distribution of firing rates in the hippocampus and entorhinal cortex. *Cell Rep.* **4**, 1010–1021.
- 18. Mizuseki, K., and Buzsáki, G. (2014). Theta oscillations decrease spike synchrony in the hippocampus and entorhinal cortex. *Philos. Trans. R. Soc. Lond. B Biol. Sci.* **369**, 20120530.
- 19. Ponce-Alvarez, A., Jouary, A., Privat, M., Deco, G., and Sumbre, G. (2018). Whole-Brain Neuronal Activity Displays Crackling Noise Dynamics. *Neuron* **100**, 1446–1459.e6.
- 20. Petermann, T., Thiagarajan, T.C., Lebedev, M.A., Nicolelis, M.A.L., Chialvo, D.R., and Plenz, D. (2009). Spontaneous cortical activity in awake monkeys composed of neuronal avalanches. *Proc. Natl. Acad. Sci. USA* **106**, 15921–15926.
- 21. Iyer, K.K., Roberts, J.A., Hellström-Westas, L., Wikström, S., Hansen Pupp, I., Ley, D., Vanhatalo, S., and Breakspear, M. (2015). Cortical burst dynamics predict clinical outcome early in extremely preterm infants. *Brain* **138**, 2206–2218.
- 22. Linkenkaer-Hansen, K., Nikouline, V.V., Palva, J.M., and Ilmoniemi, R.J. (2001). Long-range temporal correlations and scaling behavior in human brain oscillations. *J. Neurosci.* **21**, 1370–1377.
- 23. Palva, J.M., Zhigalov, A., Hirvonen, J., Korhonen, O., Linkenkaer-Hansen, K., and Palva, S. (2013). Neuronal long-range temporal correlations and avalanche dynamics are correlated with behavioral scaling laws. *Proc. Natl. Acad. Sci. USA* **110**, 3585–3590.
- 24. Shriki, O., Alstott, J., Carver, F., Holroyd, T., Henson, R.N.A., Smith, M.L., Coppola, R., Bullmore, E., and Plenz, D. (2013). Neuronal Avalanches in the Resting MEG of the Human Brain. *J. Neurosci.* **33**, 7079–7090.
- 25. Tagliazucchi, E., Balenzuela, P., Fraiman, D., and Chialvo, D.R. (2012). Criticality in large-scale brain fMRI dynamics unveiled by a novel point process analysis. *Front. Physiol.* **3**, 15.
- 26. Taleb, N.N. (2007). *The Black Swan: The Impact of the Highly Improbable* (Random House).
- 27. Barbour, B., Brunel, N., Hakim, V., and Nadal, J.-P. (2007). What can we learn from synaptic weight distributions? *Trends Neurosci.* **30**, 622–629.
- 28. Riquelme, J.L., Hemberger, M., Laurent, G., and Gjorgjieva, J. (2023). Single spikes drive sequential propagation and routing of activity in a cortical network. *Elife* **12**, e79928.
- 29. Dragoi, G. (2023). The generative grammar of the brain: a critique of internally generated representations. *Nat. Rev. Neurosci.* **1**–16.
- 30. Katz, L.C., and Shatz, C.J. (1996). Synaptic Activity and the Construction of Cortical Circuits. *Science* **274**, 1133–1138.

31. Pan, Y., and Monje, M. (2020). Activity Shapes Neural Circuit Form and Function: A Historical Perspective. *J. Neurosci.* 40, 944–954.
32. Huszár, R., Zhang, Y., Blockus, H., and Buzsáki, G. (2022). Preconfigured dynamics in the hippocampus are guided by embryonic birthdate and rate of neurogenesis. *Nat. Neurosci.* 25, 1201–1212.
33. Farooq, U., and Dragoi, G. (2019). Emergence of preconfigured and plastic time-compressed sequences in early postnatal development. *Science* 363, 168–173.
34. Dragoi, G., and Tonegawa, S. (2011). Preplay of future place cell sequences by hippocampal cellular assemblies. *Nature* 469, 397–401.
35. Malvache, A., Reichinnek, S., Villette, V., Haimerl, C., and Cossart, R. (2016). Awake hippocampal reactivations project onto orthogonal neuronal assemblies. *Science* 353, 1280–1283.
36. Logan, D.W., Brunet, L.J., Webb, W.R., Cutforth, T., Ngai, J., and Stowers, L. (2012). Learned recognition of maternal signature odors mediates the first suckling episode in mice. *Curr. Biol.* 22, 1998–2007.
37. Kostka, J.K., and Bitzenhofer, S.H. (2022). How the sense of smell influences cognition throughout life. *Neuroform* 28, 177–185.
38. Chini, M., and Hanganu-Opatz, I.L. (2021). Prefrontal Cortex Development in Health and Disease: Lessons from Rodents and Humans. *Trends Neurosci.* 44, 227–240.
39. Chini, M., Pfeffer, T., and Hanganu-Opatz, I. (2022). An increase of inhibition drives the developmental decorrelation of neural activity. *Elife* 11, e78811.
40. Kostka, J.K., and Hanganu-Opatz, I.L. (2023). Olfactory-driven beta band entrainment of limbic circuitry during neonatal development. *J. Physiol.* 601, 3605–3630.
41. Cutts, C.S., and Eglen, S.J. (2014). Detecting pairwise correlations in spike trains: an objective comparison of methods and application to the study of retinal waves. *J. Neurosci.* 34, 14288–14303.
42. Chini, M., Pöppelau, J.A., Lindemann, C., Carol-Perdiguer, L., Hnida, M., Oberländer, V., Xu, X., Ahlbeck, J., Bitzenhofer, S.H., Mulert, C., and Hanganu-Opatz, I.L. (2020). Resolving and Rescuing Developmental Miswiring in a Mouse Model of Cognitive Impairment. *Neuron* 105, 60–74.e7.
43. Chini, M., Gretenkord, S., Kostka, J.K., Pöppelau, J.A., Cornelissen, L., Berde, C.B., Hanganu-Opatz, I.L., and Bitzenhofer, S.H. (2019). Neural Correlates of Anesthesia in Newborn Mice and Humans. *Front. Neural Circuits* 13, 38.
44. Yu, Y., Burton, S.D., Tripathy, S.J., and Urban, N.N. (2015). Postnatal development attunes olfactory bulb mitral cells to high-frequency signaling. *J. Neurophysiol.* 114, 2830–2842.
45. Tufo, C., Poopalasundaram, S., Dorrego-Rivas, A., Ford, M.C., Graham, A., and Grubb, M.S. (2022). Development of the mammalian main olfactory bulb. *Dev. Camb. Engl.* 149, dev200210.
46. Claudi, F., Tyson, A.L., Petrucco, L., Margrie, T.W., Portugues, R., and Branco, T. (2021). Visualizing anatomically registered data with brainrender. *Elife* 10, e65751.
47. Golshani, P., Gonçalves, J.T., Khoshkho, S., Mostany, R., Smirnakis, S., and Portera-Cailliau, C. (2009). Internally Mediated Developmental Desynchronization of Neocortical Network Activity. *J. Neurosci.* 29, 10890–10899.
48. Rochefort, N.L., Garaschuk, O., Milos, R.I., Narushima, M., Marandi, N., Pichler, B., Kovalchuk, Y., and Konnerth, A. (2009). Sparsification of neuronal activity in the visual cortex at eye-opening. *Proc. Natl. Acad. Sci. USA* 106, 15049–15054.
49. Graf, J., Rahmati, V., Majoros, M., Witte, O.W., Geis, C., Kiebel, S.J., Holthoff, K., and Kirmse, K. (2022). Network instability dynamics drive a transient bursting period in the developing hippocampus *in vivo*. *Elife* 11, e82756.
50. Sitthiyot, T., and Holasut, K. (2020). A simple method for measuring inequality. *Palgrave Commun.* 6, 112–119.
51. Rubinov, M., and Sporns, O. (2010). Complex network measures of brain connectivity: uses and interpretations. *Neuroimage* 52, 1059–1069.
52. Antonello, P.C., Varley, T.F., Beggs, J., Porcionatto, M., Sporns, O., and Faber, J. (2022). Self-organization of *in vitro* neuronal assemblies drives to complex network topology. *Elife* 11, e74921.
53. Bassett, D.S., and Bullmore, E.T. (2017). Small-World Brain Networks Revisited. *Neuroscientist* 23, 499–516.
54. Barabási, A.-L., Bianconi, G., Bullmore, E., Burgess, M., Chung, S., Elia, S., Rad, T., George, D., Kovács, I.A., Makse, H., Nichols, T.E., et al. (2023). Neuroscience Needs Network Science. *J. Neurosci.* 43, 5989–5995.
55. Brynildsen, J.K., Rajan, K., Henderson, M.X., and Bassett, D.S. (2023). Network models to enhance the translational impact of cross-species studies. *Nat. Rev. Neurosci.* 24, 575–588.
56. Hilgetag, C.C., and Goulas, A. (2016). Is the brain really a small-world network? *Brain Struct. Funct.* 221, 2361–2366.
57. Vragović, I., Louis, E., and Díaz-Guilera, A. (2005). Efficiency of informational transfer in regular and complex networks. *Phys. Rev. E* 71, 036122.
58. Bollmann, Y., Modol, L., Tressard, T., Vorobyev, A., Dard, R., Brustlein, S., Sims, R., Bendifallah, I., Leprince, E., de Sars, V., et al. (2023). Prominent *in vivo* influence of single interneurons in the developing barrel cortex. *Nat. Neurosci.* 26, 1555–1565.
59. Markram, H., Toledo-Rodríguez, M., Wang, Y., Gupta, A., Silberberg, G., and Wu, C. (2004). Interneurons of the neocortical inhibitory system. *Nat. Rev. Neurosci.* 5, 793–807.
60. Hendry, S.H., Schwark, H.D., Jones, E.G., and Yan, J. (1987). Numbers and proportions of GABA-immunoreactive neurons in different areas of monkey cerebral cortex. *J. Neurosci.* 7, 1503–1519.
61. Dorrn, A.L., Yuan, K., Barker, A.J., Schreiner, C.E., and Froemke, R.C. (2010). Developmental sensory experience balances cortical excitation and inhibition. *Nature* 465, 932–936.
62. Vogels, T.P., Sprekeler, H., Zenke, F., Clopath, C., and Gerstner, W. (2011). Inhibitory plasticity balances excitation and inhibition in sensory pathways and memory networks. *Science* 334, 1569–1573.
63. Song, S., Miller, K.D., and Abbott, L.F. (2000). Competitive Hebbian learning through spike-timing-dependent synaptic plasticity. *Nat. Neurosci.* 3, 919–926.
64. Marques-Smith, A., Lyngholm, D., Kaufmann, A.K., Stacey, J.A., Hoerder-Suabedissen, A., Becker, E.B.E., Wilson, M.C., Molnár, Z., and Butt, S.J.B. (2016). A Transient Translaminar GABAergic Interneuron Circuit Connects Thalamocortical Recipient Layers in Neonatal Somatosensory Cortex. *Neuron* 89, 536–549.
65. Shen, J., and Colonnese, M.T. (2016). Development of Activity in the Mouse Visual Cortex. *J. Neurosci.* 36, 12259–12275.
66. Zhang, Z., Jiao, Y.-Y., and Sun, Q.-Q. (2011). Developmental maturation of excitation and inhibition balance in principle neurons across four layers of somatosensory cortex. *Neuroscience* 174, 10–25.
67. Murata, Y., and Colonnese, M.T. (2020). GABAergic interneurons excite neonatal hippocampus *in vivo*. *Sci. Adv.* 6, eaba1430.
68. Colonnese, M.T., Kaminska, A., Minlebaev, M., Milh, M., Bloem, B., Lescure, S., Moriette, G., Chiron, C., Ben-Ari, Y., and Khazipov, R. (2010). A Conserved Switch in Sensory Processing Prepares Developing Neocortex for Vision. *Neuron* 67, 480–498.
69. Sonntag, M., Englitz, B., Kopp-Scheinflug, C., and Rübsamen, R. (2009). Early postnatal development of spontaneous and acoustically evoked discharge activity of principal cells of the medial nucleus of the trapezoid body: an *in vivo* study in mice. *J. Neurosci.* 29, 9510–9520.
70. Mizuno, H., Ikezoe, K., Nakazawa, S., Sato, T., Kitamura, K., and Iwasato, T. (2018). Patchwork-Type Spontaneous Activity in Neonatal Barrel Cortex Layer 4 Transmitted via Thalamocortical Projections. *Cell Rep.* 22, 123–135.

71. Dooley, J.C., Glanz, R.M., Sokoloff, G., and Blumberg, M.S. (2020). Self-Generated Whisker Movements Drive State-Dependent Sensory Input to Developing Barrel Cortex. *Curr. Biol.* 30, 2404–2410.e4.
72. Arakawa, H., and Erzurumlu, R.S. (2015). Role of whiskers in sensorimotor development of C57BL/6 mice. *Behav. Brain Res.* 287, 146–155.
73. Akhmetshina, D., Nasretdinov, A., Zakharov, A., Valeeva, G., and Khazipov, R. (2016). The Nature of the Sensory Input to the Neonatal Rat Barrel Cortex. *J. Neurosci.* 36, 9922–9932.
74. Yang, J.-W., Kilb, W., Kirischuk, S., Unichenko, P., Stützgen, M.C., and Luhmann, H.J. (2018). Development of the whisker-to-barrel cortex system. *Curr. Opin. Neurobiol.* 53, 29–34.
75. Quast, K.B., Ung, K., Froudarakis, E., Huang, L., Herman, I., Addison, A.P., Ortiz-Guzman, J., Cordiner, K., Saggau, P., Tolias, A.S., and Arenkiel, B.R. (2017). Developmental broadening of inhibitory sensory maps. *Nat. Neurosci.* 20, 189–199.
76. Telesford, Q.K., Joyce, K.E., Hayasaka, S., Burdette, J.H., and Laurienti, P.J. (2011). The Ubiquity of Small-World Networks. *Brain Connect.* 1, 367–375.
77. Hübener, M., and Bonhoeffer, T. (2014). Neuronal plasticity: beyond the critical period. *Cell* 159, 727–737.
78. Barabási, D.L., Schuhknecht, G.F.P., and Engert, F. (2024). Functional neuronal circuits emerge in the absence of developmental activity. *Nat. Commun.* 15, 364.
79. Mitchell, K.J. (2020). Innate: How the Wiring of Our Brains Shapes Who We Are (Princeton University Press).
80. Sharf, T., van der Molen, T., Glasauer, S.M.K., Guzman, E., Buccino, A.P., Luna, G., Cheng, Z., Audouard, M., Ranasinghe, K.G., Kudo, K., et al. (2022). Functional neuronal circuitry and oscillatory dynamics in human brain organoids. *Nat. Commun.* 13, 4403.
81. Akarca, D., Dunn, A.W.E., Hornauer, P.J., Ronchi, S., Fiscella, M., Wang, C., Terrigno, M., Jagasia, R., Vérites, P.E., Mierau, S.B., et al. (2022). Homophilic wiring principles underpin neuronal network topology in vitro. Preprint at bioRxiv. <https://doi.org/10.1101/2022.03.09.483605>.
82. van der Molen, T., Spaeth, A., Chini, M., Bartram, J., Dendukuri, A., Zhang, Z., Bhaskaran-Nair, K., Blauvelt, L.J., Petzold, L.R., Hansma, P.K., et al. (2023). Protosequences in human cortical organoids model intrinsic states in the developing cortex. Preprint at bioRxiv. <https://doi.org/10.1101/2023.12.29.573646>.
83. Rößler, N., Jungentz, T., Sigler, A., Bird, A., Mittag, M., Rhee, J.S., Deller, T., Cuntz, H., Brose, N., Schwarzacher, S.W., and Jedlicka, P. (2023). Skewed distribution of spines is independent of presynaptic transmitter release and synaptic plasticity and emerges early during adult neurogenesis. *Open Biol.* 13, 230063.
84. Colonnese, M.T., Shen, J., and Murata, Y. (2017). Uncorrelated Neural Firing in Mouse Visual Cortex during Spontaneous Retinal Waves. *Front. Cell. Neurosci.* 11, 289.
85. Barabási, D.L., Beynon, T., Katona, Á., and Perez-Nieves, N. (2023). Complex computation from developmental priors. *Nat. Commun.* 14, 2226.
86. Lin, I.-C., Okun, M., Carandini, M., and Harris, K.D. (2015). The Nature of Shared Cortical Variability. *Neuron* 87, 644–656.
87. Schulz, D.P.A., Sahani, M., and Carandini, M. (2015). Five key factors determining pairwise correlations in visual cortex. *J. Neurophysiol.* 114, 1022–1033.
88. de la Rocha, J., Doiron, B., Shea-Brown, E., Josić, K., and Reyes, A. (2007). Correlation between neural spike trains increases with firing rate. *Nature* 448, 802–806.
89. Cohen, M.R., and Maunsell, J.H.R. (2009). Attention improves performance primarily by reducing interneuronal correlations. *Nat. Neurosci.* 12, 1594–1600.
90. Kohn, A., and Smith, M.A. (2005). Stimulus Dependence of Neuronal Correlation in Primary Visual Cortex of the Macaque. *J. Neurosci.* 25, 3661–3673.
91. Ecker, A.S., Berens, P., Keliris, G.A., Bethge, M., Logothetis, N.K., and Tolias, A.S. (2010). Decorrelated Neuronal Firing in Cortical Microcircuits. *Science* 327, 584–587.
92. Barreiro, A.K., and Ly, C. (2018). Investigating the Correlation-Firing Rate Relationship in Heterogeneous Recurrent Networks. *J. Math. Neurosci.* 8, 8.
93. Doiron, B., Litwin-Kumar, A., Rosenbaum, R., Ocker, G.K., and Josić, K. (2016). The mechanics of state-dependent neural correlations. *Nat. Neurosci.* 19, 383–393.
94. Luccioli, S., Angulo-Garcia, D., Cossart, R., Malvache, A., Módol, L., Sousa, V.H., Bonifazi, P., and Torcini, A. (2018). Modeling driver cells in developing neuronal networks. *PLoS Comput. Biol.* 14, e1006551.
95. Módol, L., Sousa, V.H., Malvache, A., Tressard, T., Baude, A., and Cossart, R. (2017). Spatial Embryonic Origin Delineates GABAergic Hub Neurons Driving Network Dynamics in the Developing Entorhinal Cortex. *Cereb. Cortex N. Y.* N 27, 4649–4661.
96. Bonifazi, P., Goldin, M., Picardo, M.A., Jorquera, I., Cattani, A., Bianconi, G., Represa, A., Ben-Ari, Y., and Cossart, R. (2009). GABAergic hub neurons orchestrate synchrony in developing hippocampal networks. *Science* 326, 1419–1424.
97. Kleberg, F.I., and Triesch, J. (2018). Neural oligarchy: how synaptic plasticity breeds neurons with extreme influence. Preprint at bioRxiv. <https://doi.org/10.1101/361394>.
98. Weir, K., Blanque, O., Kilb, W., Luhmann, H.J., and Sanning, A. (2014). Comparison of spike parameters from optically identified GABAergic and glutamatergic neurons in sparse cortical cultures. *Front. Cell. Neurosci.* 8, 460.
99. Gao, L., Liu, S., Wang, Y., Wu, Q., Gou, L., and Yan, J. (2023). Single-neuron analysis of dendrites and axons reveals the network organization in mouse prefrontal cortex. *Nat. Neurosci.* 26, 1111–1126.
100. Dorkenwald, S., Matsliah, A., Sterling, A.R., Schlegel, P., Yu, S., McKellar, C.E., Lin, A., Costa, M., Eichler, K., Yin, Y., et al. (2023). Neuronal wiring diagram of an adult brain. Preprint at bioRxiv. <https://doi.org/10.1101/2023.06.27.546656>.
101. Astle, D.E., Johnson, M.H., and Akarca, D. (2023). Toward computational neuroconstructivism: a framework for developmental systems neuroscience. *Trends Cogn. Sci.* 27, 726–744.
102. Hiesinger, P.R. (2021). The Self-Assembling Brain (Princeton University Press).
103. Goulas, A., Betzel, R.F., and Hilgetag, C.C. (2019). Spatiotemporal ontogeny of brain wiring. *Sci. Adv.* 5, eaav9694.
104. Juczewski, K., Koussa, J.A., Kesner, A.J., Lee, J.O., and Lovinger, D.M. (2020). Stress and behavioral correlates in the head-fixed method: stress measurements, habituation dynamics, locomotion, and motor-skill learning in mice. *Sci. Rep.* 10, 12245.
105. Kislin, M., Mugantseva, E., Molotkov, D., Kulesskaya, N., Khirug, S., Kirillkin, I., Pryazhnikov, E., Kolikova, J., Toptunov, D., Yuryev, M., et al. (2014). Flat-floored air-lifted platform: a new method for combining behavior with microscopy or electrophysiology on awake freely moving rodents. *J. Vis. Exp.* 88, e51869.
106. Steinmetz, N.A., Aydin, C., Lebedeva, A., Okun, M., Pachitariu, M., Bauza, M., Beau, M., Bhagat, J., Böhm, C., Broux, M., et al. (2021). Neuropixels 2.0: A miniaturized high-density probe for stable, long-term brain recordings. *Science* 372, eabf4588.
107. Rossant, C., Kadir, S.N., Goodman, D.F.M., Schulman, J., Hunter, M.L.D., Saleem, A.B., Grosmark, A., Belluscio, M., Denfield, G.H., Ecker, A.S., et al. (2016). Spike sorting for large, dense electrode arrays. *Nat. Neurosci.* 19, 634–641.
108. (2023). Gini Coefficient and the Lorentz Curve. <https://de.mathworks.com/matlabcentral/fileexchange/28080-gini-coefficient-and-the-lorentz-curve>.
109. Stimberg, M., Brette, R., and Goodman, D.F. (2019). Brian 2, an intuitive and efficient neural simulator. *Elife* 8, e47314.
110. Trakoshis, S., Martínez-Cañada, P., Rocchi, F., Canella, C., You, W., Chakrabarti, B., Ruigrok, A.N., Bullmore, E.T., Suckling, J., Markicevic, S., et al. (2023). A multi-scale model of the human brain. *bioRxiv*, 2023.26.05.553000.

- M., et al. (2020). Intrinsic excitation-inhibition imbalance affects medial prefrontal cortex differently in autistic men versus women. *Elife* 9, e55684.
111. Bates, D., Mächler, M., Bolker, B., and Walker, S. (2014). Fitting Linear Mixed-Effects Models using lme4. Preprint at ArXiv14065823 Stat. <https://doi.org/10.18637/jss.v067.i01>.
112. Kuznetsova, A., Brockhoff, P.B., and Christensen, R.H.B. (2017). lmerTest Package: Tests in Linear Mixed Effects Models. *J. Stat. Softw.* 82, 1–26.
113. Lüdecke, D., Ben-Shachar, M., Patil, I., Waggoner, P., and Makowski, D. (2021). performance: An R Package for Assessment, Comparison and Testing of Statistical Models. *J. Open Source Softw.* 6, 3139.
114. Lüdecke, D. (2021). sjPlot: Data Visualization for Statistics in Social Science.
115. Lenth, R.V. (2020). Emmeans: Estimated Marginal Means, Aka Least-Squares Means.

## STAR★METHODS

### KEY RESOURCES TABLE

REAGENT or RESOURCE	SOURCE	IDENTIFIER
<b>Deposited Data</b>		
Raw Data	This paper	<a href="https://gin.g-node.org/mchini/Chini_et_al_Preconfigured">https://gin.g-node.org/mchini/Chini_et_al_Preconfigured</a>
<b>Experimental Models: Organisms/Strains</b>		
Mouse: C57BL6/J	The Jackson Laboratory	Strain #: 000664
<b>Software and Algorithms</b>		
Original code	This paper	<a href="https://zenodo.org/doi/10.5281/zenodo.11091323">https://zenodo.org/doi/10.5281/zenodo.11091323</a>
Python 3.11.3	Python Software Foundation	<a href="https://www.python.org/">https://www.python.org/</a>
MATLAB R2019b	Mathworks	<a href="https://ww2.mathworks.cn/">https://ww2.mathworks.cn/</a>
R 4.3.1	The R Foundation for Statistical Computing	<a href="https://www.r-project.org/">https://www.r-project.org/</a>
<b>Other</b>		
Phase 3B Neuropixels 1.0 silicon probes	IMEC, Belgium	<a href="http://www.neuropixels.org">www.neuropixels.org</a>

### RESOURCE AVAILABILITY

#### Lead contact

Further information and requests for resources and reagents should be directed to and will be fulfilled by the lead contact, Mattia Chini ([mattia.chini@zmnh.uni-hamburg.de](mailto:mattia.chini@zmnh.uni-hamburg.de)).

#### Materials availability

The study did not generate new unique reagents.

#### Data and code availability

- SUA data that was newly generated for this study is available at the following open-access repository: [https://gin.g-node.org/mchini/Chini\\_et\\_al\\_Preconfigured](https://gin.g-node.org/mchini/Chini_et_al_Preconfigured)
- Code, processed data and statistical analysis supporting the findings of this study are available at the following open-access repository: <https://zenodo.org/doi/10.5281/zenodo.11091323>
- Any additional information required to reanalyze the data reported in this work paper is available from the [lead contact](#) upon request.

### EXPERIMENTAL MODEL AND STUDY PARTICIPANT DETAILS

All experiments were performed in compliance with the German laws and following the European Community guidelines regarding the research animal's use. All experiments were approved by the local ethical committee (G132/12, G17/015, N18/015, N19/121). Experiments were carried out on C57BL/6J mice of both sexes. Mice were housed in individual cages on a 12 h light/12 h dark cycle, and were given access to water and food *ad libitum*. P16-60 mice were housed with a minimum of two cage-mates after weaning. The mice had access to nesting material in the form of tissues and wooden gnawing material. The day of birth was considered P0. Details on the data acquisition and experimental setup of open-access datasets that were used in this project have been previously published.<sup>39,40</sup>

### METHOD DETAILS

#### *In vivo* electrophysiology in P4-12 mice

**Surgery.** *In vivo* extracellular recordings were performed from the PFC and the ventral portion of the OB of non-anesthetized P4-P12 mice. The surgery and animal preparation were analogous for the two brain regions. Before starting with the surgical procedure, a local anesthetic was applied on the neck muscles (0.5% bupivacaine/1% lidocaine). The surgery was performed under isoflurane anesthesia (induction: 5%; maintenance: 1–3%, lower for older pups, higher for younger pups). Neck muscles were severed to minimize muscle artifacts. A craniotomy over the PFC (0.5 mm anterior to bregma, 0.1–0.5 mm lateral to the midline) or the OB (0.5–0.8 mm anterior to frontonasal suture, 0.5 mm lateral to inter-nasal suture) was performed by carefully thinning the skull and then

removing it with the use of a motorized drill. Mice were head-fixed into a stereotactic frame and kept on a heated ( $37^{\circ}$ ) surface surrounded by cotton wool throughout the entire recording. To record from the PFC, a Neuropixels probe 1.0 phase 3B (Imec, Belgium) was slowly vertically inserted (angle  $0^{\circ}$ ) into the frontal lobe (insertion time 20–30 min), at a depth varying between 2.6 and 4 mm depending on the age of the animal. Due to the small size of the brain, in younger animals, not all 384 recording channels were inserted in the brain. The tip of the probe was used as reference. To record from the OB, a single-shank silicon probe (NeuroNexus, MI, USA) with 16 recording sites and 50  $\mu\text{m}$  inter-site spacing was vertically inserted (angle  $0^{\circ}$ ) at a depth varying between 1.0 and 2.0 mm. A silver wire inserted in the cerebellum was used as reference. Both probe types were inserted using a micromanipulator. Before signal acquisition, mice were allowed to recover for  $\sim$ 45 min, to maximize the quality and stability of the recording as well as single units' yield.

**Signal acquisition.** For PFC recordings, signals from the bottom 384 channels were recorded at a 30 kHz using the Neuropixels head-stage 1.0 and Neuropixels 1.0 PXle acquisition system (Imec, Belgium). The SUA signal was acquired through the OpenEphys interface and the Neuropixels plugin (AP gain = 500, AP Filter Cut = ON). For OB recordings, signals were band-pass filtered (0.1–9 kHz) and digitized (32 kHz) by a multichannel amplifier (Digital Lynx SX; Neuralynx, Bozeman, MO, USA) and acquired through the Cheetah acquisition software (Neuralynx, Bozeman, MO, USA).

**Histology.** Epifluorescence images of coronal brain sections were acquired postmortem to reconstruct the position of the Dil-stained recording electrode. Only mice in which the electrodes were placed in the correct position were kept for further analysis.

#### **In vivo electrophysiology in P16-60 mice**

**Surgery.** Acute *In vivo* extracellular recordings were performed from the PFC of awake, head-fixed mice of both sexes. Before starting with the surgical procedure to implant a metal head-plate (Neurotar, Helsinki, Finland) for head-fixation, buprenorphine (0.5 mg/kg bw) was injected subcutaneously. The surgery was performed under isoflurane anesthesia (induction: 5%; maintenance: 2.5%). Anesthesia depth was confirmed with the paw withdrawal reflex. Eyes were covered with an ointment (Vidisic, Bausch + Lomb, Berlin, Germany) to prevent them from drying out. After disinfection with Betasisodona, the scalp was removed from the top of the head and the edges treated for analgesia with application of a Lidocain/Bupivacain mixture (0.5% bupivacain/1% lidocaine). A craniotomy was performed to make the mPFC (0.5–2.0 mm anterior to bregma, 0.1–0.5 mm right to the midline) accessible for recordings. A synthetic window was fixed to the skull around the craniotomy to be able to protect the tissue with Kwik-Cast sealant (World Precision Instruments, Friedberg, Germany). A silver wire, serving as a ground and reference electrode, was inserted between the skull and cerebellum. The metal head-plate was attached to the skull with dental cement. For recovery from anesthesia, mice were placed in a cage on a heating mat and after being fully awake, they were put back into their home cage with their cage mates. For further analgesia, Metacam (0.5 mg/mL, Boehringer-Ingelheim, Germany) was mixed into soft food and provided for 48 h after the surgery.

**Training and signal acquisition.** After recovery from the surgery, mice were accustomed to the head-fixation system and trained to move the air-lifted carbon cage from the MobileHomeCage system (Neurotar, Helsinki, Finland). To perform electrophysiological recordings, the craniotomy was uncovered and an electrode (NeuroNexus, MI, USA) was stereotactically inserted into the mPFC (one-shank, A1x16-channel, 100  $\mu\text{m}$ -spaced, 2.0 mm deep). The signal was acquired for 30–40 min. Extracellular signals were band-pass filtered (0.1–9000 Hz) and digitized (32 kHz) with a multichannel extracellular amplifier (Digital Lynx SX; Neuralynx, Bozeman, MO, USA). During the electrophysiological recordings, mice were head-fixed and able to move the air-lifted platform, mimicking free locomotion.<sup>104,105</sup> All mice showed a combination of voluntary movement and quiet wakefulness. To ensure that we analyzed data from a consistent behavioral state, we excluded movement periods from further analysis. For a subset of mice, we also recorded eye movement and pupil size, and did not detect any sleep epoch. We focused our analysis on periods of quiet wakefulness because these behavioral epochs were much more abundant and displayed a higher signal quality. Multiple electrophysiological recordings were performed in the same animal, with a minimal recovery period of two days in between the recordings. Between recording sessions, mice were housed in their standard housing conditions and did not perform any particular behavioral task.

**Histology.** Epifluorescence images of coronal brain sections were acquired postmortem to reconstruct the position of the recording electrode. To this aim, after the last recording, a Dil-coated electrode was inserted. Only mice in which the electrodes were placed in the correct position were kept for further analysis.

## **QUANTIFICATION AND STATISTICAL ANALYSIS**

#### **Spike sorting**

P4-12 PFC recordings were spike-sorted with Kilosort 2.5<sup>106</sup> (fshigh = 500, minFR = 0.001, spkTh = -4, sig = 20, nblocks = 5). All other recordings were spike-sorted with Klusta.<sup>107</sup> Automatically-obtained clusters were manually curated using phy (<https://github.com/cortex-lab/phy>).

#### **SUA firing statistics and shape distribution parameters**

**Firing rate.** Firing rate (in Hz) was computed as the number of spikes divided by the total recording length in seconds.

### Spike-Time Tiling Coefficient (STTC)

The STTC (timescale of 10 ms) was computed as follows<sup>39,41</sup>:

$$STTC = \frac{1}{2} \left( \frac{P_A - T_B}{1 - P_A T_B} + \frac{P_B - T_A}{1 - P_B T_A} \right) \quad (\text{Equation 2})$$

where  $P_A$  is the proportion of spikes of spike train A that occurs within  $\pm\Delta t$  of a spike train B spike.  $T_A$  is the proportion of time that occurs within (is “tiled” by)  $\pm\Delta t$  from spikes of spike train A. The same applies for  $P_B$  and  $T_B$ .  $\pm\Delta t$  is the lag parameter and was set at 10 ms.

### Skewness

Skewness was computed using the homonymous MATLAB function *skewness* as:

$$\text{skewness} = E \left[ \left( \frac{(X - \mu)}{\sigma} \right)^3 \right] \quad (\text{Equation 3})$$

Where X is the random variable of interest,  $\mu$  is its mean,  $\sigma$  its standard deviation, and E is the expectation operator.

### Kurtosis

Kurtosis was computed using the homonymous MATLAB function *kurtosis* as:

$$\text{kurtosis} = E \left[ \left( \frac{(X - \mu)}{\sigma} \right)^4 \right] \quad (\text{Equation 4})$$

Where X is the random variable of interest,  $\mu$  is its mean,  $\sigma$  its standard deviation, and E is the expectation operator.

### Gini coefficient

The Gini coefficient was computed using the MATLAB function *gini*<sup>108</sup>. The Gini coefficient is calculated by taking the ratio of the area that lies between the line of equality and the Lorenz curve, over the total area under the line of equality.

### Complex network properties

To calculate the network properties of the developing brain, we utilized symmetrical STTC matrices. The pre-processing consisted of thresholding and binarization. To threshold the data, we computed surrogate spiking data for each mouse individually. To account for the slow co-modulation of firing rates that is typical of the developing brain, we generated surrogate spiking data by leaving the timing of spikes unaffected and shuffling the identity of the neuron that emitted the spike. This pseudo-randomization thus generated surrogate spike vectors while preserving the population rate. Using these spike vectors, we then computed at least 1000 STTC values on shuffled data, and used the 90<sup>th</sup> percentile value to threshold and binarize the real-data STTC matrices. The binary and undirected matrices were then analyzed with the MATLAB Brain Connectivity Toolbox.<sup>51</sup>

The clustering coefficient and transitivity of the matrices were extracted with the *clustering\_coef\_bu* and *transitivity\_bu* functions, respectively. To compute the characteristic path length, we first computed the distance matrix (*distance\_bin*) and then computed the characteristic path length (*charpath*) without including distances on the main diagonal and infinite distances. All these values were normalized by dividing them with a corresponding “null” value that was computed by generating 100 synthetic random networks (*makerandClJ\_und*), extracting the same parameters for each iteration, and computing the average. Small-worldness was computed by dividing the normalized clustering coefficient by the normalized characteristic path length.

The four “hubness” parameters that we used to compute the composite “hubness score” were also extracted with the same MATLAB toolbox. For each node individually, we computed its total amount of edges (i.e., its degree, using *degrees\_und*), its total amount of weights (*strengths\_und*, this is the only parameter that was computed on weighted and not binary matrices), its betweenness centrality (*betweenness\_bin*, after using *weight\_conversion* and ‘lengths’) and its closeness centrality (the inverse of the node’s average distance computed with *distance\_bin*).

### Neural network modeling

All simulations were performed using Brian2 for Python3.7.<sup>109</sup>

### General structural neural network architecture

The architecture of the network<sup>39,110</sup> is schematically illustrated in Figures 6A–6C. The network was composed of 400 conductance-based leaky integrate-and-fire neurons, 80% of which were excitatory (PYRs) ( $N = 320$ ) and 20% were inhibitory (INs) ( $N = 80$ ). PYRs were simulated with outgoing excitatory synapses and INs with outgoing inhibitory synapses. Excitatory (PYR → PYR, PYR → IN) and inhibitory (IN → IN and IN → PYR) synapses were simulated as AMPA and GABA conductances, respectively. Due to the near-instantaneous rise times of AMPA- and GABA-mediated currents (both typically <0.5 ms), we opted to neglect these in the simulations. Synaptic transmission was assumed to be instantaneous (i.e., with zero delay).

The dynamics of each excitatory and inhibitory cell were governed by the following stochastic differential equation:

$$C_m \frac{dV_m}{dt} = -g_L(V_m - V_L) - g_{\text{AMPA}}(V_m - E_{\text{AMPA}}) - g_{\text{GABA}}(V_m - E_{\text{GABA}}) + \sigma\xi \quad (\text{Equation 5})$$

with

$$\frac{dg_{AMPA}}{dt} = -\frac{g_{AMPA}}{\tau_{AMPA}} \quad (\text{Equation 6})$$

and

$$\frac{dg_{GABA}}{dt} = -\frac{g_{GABA}}{\tau_{GABA}} \quad (\text{Equation 7})$$

where  $V_m$  is the membrane potential,  $V_L$  is the leak membrane potential and  $E_{AMPA}$  and  $E_{GABA}$  denote the AMPA and GABA current reversal potentials, respectively. The synaptic conductance parameters and the corresponding decay time constants are denoted by  $g_{AMPA}$ ,  $g_{GABA}$  and  $\tau_{AMPA}$ ,  $\tau_{GABA}$ , respectively.  $\sigma\xi$  is a noise term that is generated by an Ornstein-Uhlenbeck process with zero mean. The networks were simulated for a duration of 10 s (simulations without plasticity) or 50 s (simulations with plasticity). All simulations were performed with a time step ( $dt$ ) of 0.1 ms and integrated with Euler's method. All parameter values/ranges used in the simulations are listed in [Table S1](#).

#### Random variables

To avoid choosing an arbitrary structural neural network architecture, a number of parameters were treated as "random variables" and systematically varied across a biologically-constrained range. These parameters included: 1) the noisy input (Ornstein-Uhlenbeck process) that was used to independently drive PYRs and INs; 2) the mean probability with which neurons were connected, which was the same for all possible population combinations: i) PYR-PYR, ii) PYR-IN, iii) IN-PYR, iv) IN-IN; 3) the mean size of excitatory and inhibitory synaptic weights.

#### Synaptic parameters

In these networks, we studied the influence on the simulated SUA statistics exerted by three synaptic parameters: whether the size of synapses followed a normal or a log-normal distribution, whether the number of synapses of individual neurons followed a normal or a log-normal distribution, and whether the number of dendritic and axonic (incoming and outgoing) synapses were correlated or uncorrelated with each other. The 2 possible configurations for the 3 synaptic parameters resulted in  $2^3 = 8$  different network types, of which we simulated 1000 each. These 3 synaptic parameters were simultaneously varied for the entire network and not in a neuronal population-specific manner.

#### Number of synapses and correlation between dendritic and axonic synapses

We first generated a normal (mean = 1, std = 1/4) or log-normal (mean of the underlying normal = 0, std of the underlying normal = 0.5) relative distribution of the number of connections that was normalized to have a sum = 1. To account for the different number of connections in different simulations (see previous paragraph *Random variables*), the relative distribution was then scaled by the total amount of connections between the pre- and post-synaptic population according to:

$$\text{tot. connections} = N_{pre} * N_{post} * \text{mean connectivity} \quad (\text{Equation 8})$$

Where  $N_{pre}$  is the number of presynaptic neurons (PYRs or INs),  $N_{post}$  is the number of postsynaptic neurons (PYRs or INs) and *mean connectivity* is a parameter that is randomly varied between simulations. Please note that, due to the normalization, the fact that the two original distributions have a different mean is irrelevant. This process was repeated until the simulated number of connections had no negative values and no values exceeded the maximum amount of possible synaptic partners ( $N_{pre}$  or  $N_{post}$ ). In the case of uncorrelated incoming and outgoing number of synapses, the same procedure was then repeated for the distribution of pre/post-synaptic partners. In simulations in which the number of incoming and outgoing synapses was correlated, the number of pre-synaptic connections was drawn using a random number generator (numpy function *rng.choice*), in which the maximum value (a, following the nomenclature of *rng.choice*) was set equal to the number of pre/post-synaptic neurons, the number of values to draw was equal to *tot. connections* (size, following the nomenclature of *rng.choice*) and the probabilities associated with each pre-synaptic neuron were equal to the number of outgoing connections of that neuron (p, following the nomenclature of *rng.choice*). This resulted in a Pearson correlation of the number of incoming and outgoing synapses  $\sim 0.85$ , in line with what has been described in Drosophila.<sup>100</sup> Finally, to generate a connectivity matrix in which each neuron had the desired amount of incoming and outgoing connections, we used the *directed\_havel\_hakimi\_graph* function from the *networkx* python package.

#### Size of synapses

The distribution of synaptic sizes was simulated according to a normal (mean =  $\sqrt[3]{e}$ , std = 1/2) or log-normal (mean of the underlying normal = 0, std of the underlying normal = 1) distribution. Please note that it can be analytically shown that the two distributions have the same mean. These distributions were then scaled by different scalars (see [Table S1](#)) according to the specifics of the connected populations.

#### Synaptic plasticity

For simulations with synaptic plasticity, synaptic parameters were set to their extreme configuration (lognormal distribution of synaptic weights and number, and correlated amount of incoming and outgoing number of synapses). A set of other parameters controlling the structural network architecture was systematically varied across a biologically-constrained range, analogously to simulations without synaptic plasticity (see *Random variables*). In these networks, we first simulated 10s with frozen synaptic weights, and 40s with synaptic plasticity.

PYR-PYR excitatory synapses were plastic according to a classic asymmetric Hebbian plasticity rule<sup>63</sup> that can be summarized as follows:

$$\frac{dW}{dt} = \frac{\eta(\text{pre} * \text{post})}{\tau_{STDP}} \quad (\text{Equation 9})$$

Where  $W$  is a PYR-PYR synaptic weight,  $\text{pre}$  and  $\text{post}$  are the pre- and postsynaptic activity,  $\eta$  is the learning rate, and  $\tau_{STDP}$  is the decay time constant of the plasticity rule.

In practice, synaptic weights from a pre-synaptic neuron  $i$  to a post-synaptic neuron  $j$  ( $W_{ij}$ ) were updated at every pre- and post-synaptic event occurring at time  $t_i$  and  $t_j$  such that:

$$W_{ij} \rightarrow W_{ij} + \eta x_i \text{ for presynaptic spikes at time } t_i \quad (\text{Equation 10})$$

$$W_{ij} \rightarrow W_{ij} + \eta x_j \text{ for postsynaptic spikes at time } t_j \quad (\text{Equation 11})$$

Where  $x_i$  and  $x_j$  are the pre- and post-synaptic trace.

$x_i$  was updated with each spike  $x_i \rightarrow x_i + 0.01$  and decayed according to:

$$\frac{dx_i}{dt} = - \frac{x_i}{\tau_{STDP}} \quad (\text{Equation 12})$$

$x_j$  was updated with each spike  $x_j \rightarrow x_j - 0.01$  and decayed according to:

$$\frac{dx_j}{dt} = - \frac{x_j}{\tau_{STDP}} \quad (\text{Equation 13})$$

Synaptic weights were clipped within the 0–10 range.

IN-PYR inhibitory synapses were plastic according to a symmetric plasticity rule.<sup>62</sup> This rule can be summarized as follows:

$$\frac{dW}{dt} = \frac{\eta(\text{pre} * \text{post} - \alpha * \text{pre})}{\tau_{STDP}} \quad (\text{Equation 14})$$

Where  $W$  is an IN-PYR synaptic weight,  $\text{pre}$  and  $\text{post}$  are the pre- and postsynaptic activity,  $\alpha$  is the target rate for the postsynaptic PYR, drawn from a log-normal distribution,  $\eta$  is the learning rate, and  $\tau_{STDP}$  is the decay time constant of the plasticity rule.

Synaptic weights  $W_{ij}$  were updated at every pre- and post-synaptic event occurring at time  $t_i$  and  $t_j$  such that:

$$W_{ij} \rightarrow W_{ij} + \eta(x_i - \alpha) \text{ for presynaptic spikes at time } t_i \quad (\text{Equation 15})$$

$$W_{ij} \rightarrow W_{ij} + \eta x_j \text{ for postsynaptic spikes at time } t_j \quad (\text{Equation 16})$$

Where  $x_i$  and  $x_j$  are the pre- and post-synaptic trace that increased with each spike  $x \rightarrow x + 1$  and decayed according to:

$$\frac{dx}{dt} = - \frac{x}{\tau_{STDP}} \quad (\text{Equation 17})$$

Synaptic weights were clipped within the 0–100 range.

#### **Simulated SUA statistics and quality of model fit**

For each network, we extracted the simulated spike times and computed the same 7 parameters as for the experimental data (described in *SUA firing statistics and shape distribution parameters*): skewness, kurtosis and Gini coefficient of firing rate and STTC, and the correlation between the log-transformed firing rate and STTC. To compute the quality of the model fit, we extracted the median of these 7 parameters from the P4-12 PFC dataset. For each simulation, we then computed the Euclidian distance (MATLAB function *pdist*) between the median of the experimental data and the 7D coordinates of that specific simulation. To ensure that each metric contributed equally to the distance from the experimental data, kurtosis and skewness of firing rate and STTC were divided by their maximum value. This normalized them to a range comprised between 0 and 1, as the Gini coefficient.

#### **Statistical modeling**

Statistical modeling was carried out in the R environment. All the scripts and the processed data on which the analysis is based are available on the following github repository: <https://zenodo.org/doi/10.5281/zenodo.11091323>.

Nested data (Figures 1, 4, and 6) were analyzed with (generalized) linear mixed-effects models (*lmer* and *glmer* functions of the *lme4* R package<sup>111</sup>) with “mouse” as random effect. Non-nested data were analyzed with linear models (*lm* function). Regression on data that was better fit by an exponential curve (Figure 1) was carried out with a generalized linear mixed-effect models with the following parameters: family = Gamma, link = log. For ease of interpretability and consistency with the other distribution shape parameters, kurtosis of firing rate and STTC, which followed an approximately log-normal distribution, was instead log-transformed and analyzed with a linear model.

Statistical significance for linear mixed-effects models was computed with the *lmerTest* R package<sup>112</sup> and the *summary* (type III sums of squares) R function. Statistical significance for linear models was computed with the *summary* R function.

When possible, model selection was performed according to experimental design. When this was not possible, models were compared using the *compare\_performance* function of the *performance* R package,<sup>113</sup> and model choice was based on an holistic comparison of AIC, BIC, RMSE and R2.

Model output was plotted with the *plot\_model* (type = 'pred') function of the *sjPlot* R package.<sup>114</sup> 95% C.I. were computed using the *confint* R function.

Post hoc analysis was carried out using the *emmeans* and *emtrends* functions of the *emmeans* R package.<sup>115</sup>